الجمهوريـــــة الجزائريـــــة الديموقراطيـــــة الشعبيـــــة
PEOPLE'S DEMOCRATIC REPUBLIC OF ALGERIA
وزارة التـــعـليـم العـــالي والبـحث العـــلـمـي
Ministry of Higher Education and Scientific Research

UNIVERSITY OF SAÏDA - DR. MOULAY TAHAR جـــامعة سعيدة – د. مولاي الطاهر

Faculty of Science and Technology **كلية العلوم والتكنولوجيا**

Department of Materials Science **قسم علوم المادة**

DISSERTATION

Prepared for the purpose of obtaining a Master's degree in Physics

Specialization: Materials Physics

Title:

Design and Modeling of Spinel Compound Co_2MnO_4 using the FP-LAPW Method: Exploring Structural, and Magneto-Electronic Properties for Spintronic Applications

---

Presented by:

NOUARI Faycal Abdelnaceur

Defended on: 22/06/2025 before the jury composed of:

Dr. Malika HACHEMAOUI	University of Saïda - Dr MOULAY Tahar	President
Dr. Friha KHELFAOUI	University of Saïda - Dr MOULAY Tahar	Supervisor
Dr. Hayat HOCINE	University of Saïda - Dr MOULAY Tahar	Examinator

Academic Year 2024/2025

DEDICATION

To her who, after God, was the reason for all my successes,

To her who instilled in me the love of knowledge and work,

To her who was my help and support throughout all stages of my life...

To my **dear mother**, my source of strength and inspiration,

who taught me that ambition knows no bounds

and that diligence is the key to every success.

To my **dear father**, my support, and the source of my inspiration

, ambition, and successes.

To my **brothers and sisters**, who have been and continue

to be an inexhaustible wellspring of support and the best help to me.

To my **dear friends and colleagues**, who shared my joys

and difficult moments, and contributed

to enriching this experience.

To **myself**, who challenged hardships and

persevered to achieve this accomplishment.

I dedicate this humble work to everyone who left their mark

on my academic and professional journey.

To my **dear teacher Khelfaoui Friha**.

Acknowledgements and Gratitude

First, I would like to express my deepest gratitude to **Dr. Friha KHELFAOUI**, my supervisor, for his invaluable guidance, continuous support, and insightful advice throughout the entire duration of this work. His expertise and encouragement have been instrumental in the realization of this dissertation.

I am sincerely thankful to **Dr. Malika HACHEMAOUI**, President of the jury, for her thoughtful remarks, constructive feedback, and for accepting to preside over the defense of this work.

My sincere appreciation also goes to **Dr. Hayat HOCINE**, examiner, for her careful evaluation of the manuscript and for the enriching discussions during the defense.

I would also like to extend my gratitude to all the faculty members, staff, and colleagues at the **University of Saïda – Dr Moulay Tahar**, especially those in the Department of Physics and the Laboratory of Physico-Chemical Studies, for creating a stimulating and supportive academic environment.

Finally, I thank my family and friends for their patience, encouragement, and unwavering support throughout this academic journey

Table of contents

List of figures

GENERAL INTRODUCTION

General introduction

Spinel materials constitute a remarkable class of compounds that have garnered significant interest due to their unique structural and functional properties [1-3]. These properties critically depend on several factors; particularly the specific metal ions incorporated within the structure[4] their arrangement within the lattice and the overall crystal structure itself. These materials exhibit diverse atomic and electronic configurations[5], resulting in exceptional electronic, optical[6, 7], magnetic, and catalytic properties[8-11]. This remarkable spectrum of properties endows spinel materials with exceptional versatility, enabling applications across diverse technological fields. These include data storage[12], high-frequency electronic devices[13], dielectric materials, transparent conducting oxides, and laser technologies[14]. These materials also serve as functional components in sensor technologies and super capacitor electrodes[15], with additional applications spanning superconductivity, biotechnology, biomedical engineering, and renewable energy systems[16-19]. The chemical composition of spinel compounds follows the general formula AB_2O_4, where A represents divalent cations (A^{2+}) occupying tetrahedral sites and B denotes trivalent cations (B^{3+}) in octahedral coordination. These materials exhibit two primary structural configurations: normal and inverse spinel arrangements, distinguished by their cation distribution among the available crystallographic sites[20]. The normal spinel structure, which is the most common and was first elucidated in 1915 by Bragg and Nishikawa, exhibits a geometric arrangement in which A atoms occupy tetrahedral coordination sites, while B atoms reside in octahedral sites[21]. In contrast, the inverse spinel configuration, as characterized by Barth and Posnjak [22], deviates from this standard arrangement. In the inverse structure, denoted as $BABO_4$, B atoms occupy the tetrahedral sites, while the octahedral sites are shared equally between A and B atoms.

Driven by advances in the field, research has shifted focus to ternary spinel oxides [8]. These oxides are characterized by three distinct metal cations occupying both tetrahedral and octahedral sites within the crystalline structure. Such multicomponent materials offer an even broader range of tunable properties [23-25], as demonstrated by recent investigations into 3d transition metal-based ternary spinel oxides using density functional theory (DFT). This approach has enabled researchers to decipher critical factors influencing lithium-ion battery cathodes, including cation site preferences, delithiation voltages, and thermodynamic

stability[26]. These parameters are essential for developing high-performance, practical cathode materials.

In our case, we are studying the Cobalt manganese oxide (Co_2MnO_4) which stands out among spinel-type materials due to its unique properties and versatile applications [27-29]. This compound adopts an inverse spinel structure ($Co^{2+}Co^{3+}Mn^{3+}O_4$) and exhibits ferrimagnetic behavior [30]. Its physicochemical characteristics—including magnetic performance—are highly dependent on elemental composition and crystal lattice **arrangement** [31].Extensive research has explored Co_2MnO_4's magnetic properties and potential uses, particularly in advanced functional materials [32, 33]. Studies also highlight how **elemental substitution** (e.g., doping or stoichiometric modifications) can significantly alter its magnetic response [34-36], offering avenues for tailored material design.

To explore the untapped potential of this spinel compound class and systematically characterize their properties for optimized synthesis, investigations were conducted using the full-potential linearized augmented plane wave (FP-LAPW) method.

This approach enabled comprehensive verification of stability and accurate prediction of elastic properties, while elucidating the structural, electronic, and magnetic characteristics of the Co_2MnO_4 compound. Our investigations employed computational platformsWien2k [37].

Electronic structure analysis incorporated the Generalized Gradient Approximation (GGA) [38]. This multi-methodological framework provided robust understanding and predictive capability regarding the physical properties of this novel material.

This manuscript is organized into three chapters. The foundational chapter establishes our theoretical framework through comprehensive implementation of quantum mechanical computational methods within density functional theory (DFT), specifically, the Full-Potential Linearized Augmented Plane Wave (FP-LAPW) method. Chapter II elaborates these theoretical foundations in detail. Chapter III presents and analyzes our research results and discussions. Chapter I, which provides a comprehensive review of, precedes these core technical chapters: Fundamental principles of spinel materials, their characteristic physical properties and Current technological applications.

The work concludes with a synthesis section that systematically summarizes key findings, highlights the most significant results, proposes concrete future research directions and Outlines promising technological perspectives.

CHAPTER I:

OVERVIEW OF SPINEL MATERIALS AND THEIR TECHNOLOGICAL APPLICATIONS

1.1.Introduction

Spinel compounds, with the general formula AB_2X_4, represent an important class of materials known for their versatile structural, electrical, magnetic, and optical properties. These materials crystallize in a cubic close-packed lattice where divalent (A) and trivalent (B) cations occupy tetrahedral and octahedral sites, respectively, within a framework of anions (X), typically oxygen, sulfur, or selenium. The flexibility in cation substitution and distribution allows for the fine-tuning of properties, making spinels suitable for a wide range of technological applications.

Due to their chemical stability, high melting points, and tunable electronic characteristics, spinel-type materials have been extensively studied and utilized in various fields, including catalysis, energy storage, magnetic devices, sensors, and optoelectronic applications. Recent advancements in synthesis and characterization techniques have further enhanced the understanding of spinel structures, enabling the design of novel materials with optimized functionalities.

This chapter provides a comprehensive overview of spinel compounds, beginning with their structural features and classification, followed by a discussion of key physical properties. The latter sections focus on specific applications, highlighting the role of spinel materials in modern technologies and emerging research areas.

1.2.Crystal Structure of Spinels

The general formula AB_2O_4 adopts a spinel structure analogous to that of natural spinel, $MgAl_2O_4$[39]. This cubic structure, belonging to the $Fd\bar{3}m$ space group (No. 227), features a close-packed arrangement of oxygen ions forming a face-centered cubic lattice. Within this framework, cations are distributed between two distinct coordination sites: octahedral (*Oh*) and tetrahedral (*Td*). This specific cation distribution results in eight AB_2O_4 unit motifs (or octants) per unit cell. These motifs highlight the arrangement of A^{2+} and B^{3+} cations around O^{2-} anions, illustrating the complexity of the spinel structure. The unit cell is rhombohedral and contains two formula units of AB_2O_4. However, since this cell is not the most convenient for describing the structure, we instead analyze the smallest cubic multiple cell. This cubic cell comprises 32 oxygen atoms, which define 32 B sites and 64 A sites. Only 8 A sites and 16 B sites are occupied by cations. Consequently, the smallest cubic cell contains 8 formula units of AB_2O_4 [40]

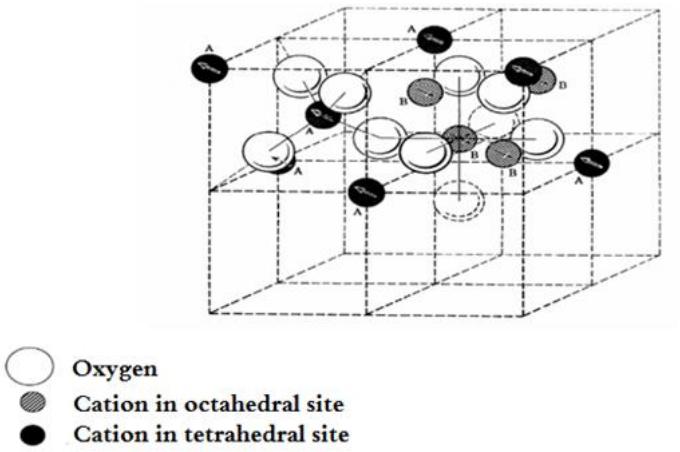

Figure 1.1. Unit cell of the AB_2O_4 spinel structure

To describe the structure, the unit cell with lattice parameter *a* is divided into eight smaller cubes (octants) with edge lengths of *a/2, a/2,* and *a/2*. Figure I-1 shows the cation and anion positions in two adjacent octants. The oxygen anions are identically arranged in all octants, forming the vertices of a tetrahedron inscribed within a smaller cube of edge length $\frac{a}{4}, \frac{a}{4}, \text{and } a/4$ [41]. The occupied A sites are distributed in the center or every alternate octantand at the half of the vertices across all octant. Within the cubic unit cell, the A sites constitute two face-centered cubic (FCC) sublattices, offset from each other by $a\sqrt{3}/4$ along the [111] direction. The occupied B sites are located in every second octant. Similar to the oxygen anions, they are positioned at one-quarter of the octant's space diagonal from four of its eight vertices, forming a tetrahedron inscribed within a cubic subcell of edge length a/4 [42].

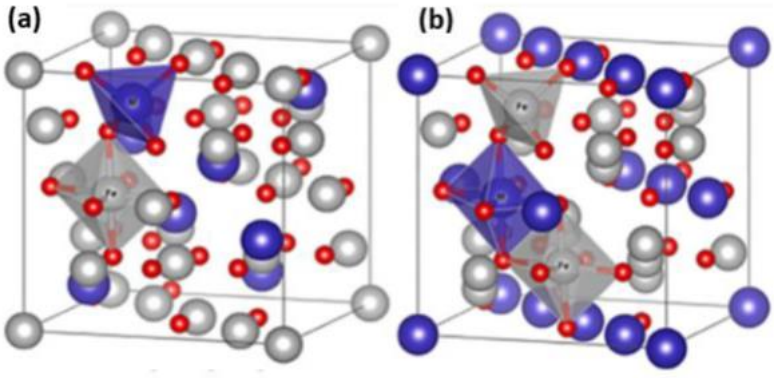

Figure 1.2: (a) Normal spinel structure, (b) Inverse spinel structure[43].

Generally, oxygen atoms (anions) are not precisely located at the FCC (face-centered cubic) sublattice positions. The exact position of the oxygen ions is determined by the parameter (u). This parameter represents the distance between an O^{2-} anion and the cations

in a tetrahedral (Td) site [44]. The parameter (u) is expressed as a fraction of the lattice parameter (a).

In the ideal structure, (u) equals 0.375a. However, this ideal configuration is almost never achieved, and for most known spinels, the value of (u) lies between 0.375 and 0.385 [45]. The presence of O^{2-} ions along with tetrahedral and octahedral sites within the face-centered cubic (FCC) lattice allows for variable ionic distributions among these nonequivalent sites. These cationic arrangements can be described by a parameter known as the inversion degree (λ), which represents the percentage of divalent ions occupying octahedral sites.

The general formula for a spinel structure is written as follows (by convention, octahedral sites are enclosed in square brackets) [46]$A^{2}_{1-2\lambda}\ B^{3+}_{2\lambda}\ [A^{2+}_{2\lambda}\ B^{3+}_{2-2\lambda}]$, Where λ represents the inversion degree.

- ✓ For λ=0, the spinel is referred to as 'normal' with the formula $A[B_2]O_4$.
- ✓ For λ=0.33, the spinel is statistically disordered, or partially inverse (mixed).
- ✓ For λ=0.5, the spinel is referred to as 'inverse' with the formula $B[AB]O_4$.

Spinel structures can be classified into two types based on cation distribution: normal spinels and inverse spinels. In a normal spinel $(A[B_2]O_4)$ the A^{2+} cations occupy tetrahedral sites (Td) and B^{3+} cations occupy octahedral sites (Oh). However in an inverse spinel $(B[AB]O_4)$ half of the B^{3+} cations occupy tetrahedral sites (Td) and the remaining A^{2+} and B^{3+} cations jointly occupy octahedral sites (Oh).

1.3.Spinel Ferrites

Spinel ferrites, commonly referred to simply as ferrites, are primarily composed of trivalent iron and oxygen. Their general chemical formula is MFe_2O_4, where M represents a divalent metal cation, with iron present in the trivalent state [47].The most relevant ferrites for various applications are complex compounds where M represents a combination of divalent ions such $as\ Mn^{2+}, Ni^{2+}, Zn^{2+}, Fe^{2+}, Co^{2+}, and\ Cu^{2+}$.

Ferrites, due to their lack of a preferred magnetization direction, are classified as 'soft' magnetic materials [48].This indicates that their magnetization direction can be readily altered by applying an external magnetic field [49].The magnetic properties of ferrites

depend not only on the metal ions occupying interstitial sites but also on their cationic distribution. These characteristics make ferrites valuable for diverse applications, including magnetic storage media, microwave devices, and magnetic sensors [50, 51].

1.4.Types of Magnetism

Magnetism arises from the motion of electric charges, particularly the spin and orbital motion of electrons within atoms. In solid-state materials, the collective behavior of these magnetic moments gives rise to various forms of magnetism, each characterized by distinct interactions between atomic moments and their responses to external magnetic fields. Understanding these types is essential for interpreting the magnetic behavior of spinel compounds and designing materials for specific applications such as magnetic storage, spintronics, and sensors (see **Figure 1.3**).

1.4.1. **Ferromagnetism**

Ferromagnetic materials exhibit spontaneous magnetization, wherein the magnetic moments of constituent atoms or ions align parallel to each other even in the absence of an external magnetic field. This parallel alignment generates a permanent net magnetization. The Curie temperature (Tc) represents the critical threshold above which the material loses its permanent magnetization and transitions to paramagnetic behavior. At this temperature, thermal energy randomizes the magnetic moment orientations through increased thermal fluctuations.

1.4.2. Antiferromagnetism

Antiferromagnetic materials exhibit antiparallel coupling of atomic or ionic magnetic moments. Below the Néel temperature (T_N), these moments adopt an antiparallel alignment, resulting in complete cancellation of net magnetization. Such materials demonstrate low magnetic susceptibility and fundamentally distinct magnetic response compared to ferromagnetic systems. The Néel temperature represents the critical transition point where the material loses its antiparallel magnetic ordering and undergoes a paramagnetic phase transition. Above T_N, thermal energy randomizes the magnetic moment orientations through increased thermal fluctuations.

1.4.3. Ferrimagnetism

Ferrimagnetic materials are characterized by antiparallel alignment of ionic magnetic moments, but unlike antiferromagnetic systems, these moments do not completely cancel due to unequal moment magnitudes. This imbalance creates a spontaneous net magnetization [52]. Such magnetic ordering is characteristic of ferrites, which find extensive technological applications. Similar to ferromagnetic materials, ferrimagnets undergo a paramagnetic transition above their Curie temperature (T_C). However, ferrimagnetic systems may additionally exhibit a compensation temperature (T_{comp}) where the net magnetization vanishes prior to reaching T_C due to opposing sublattice magnetizations.

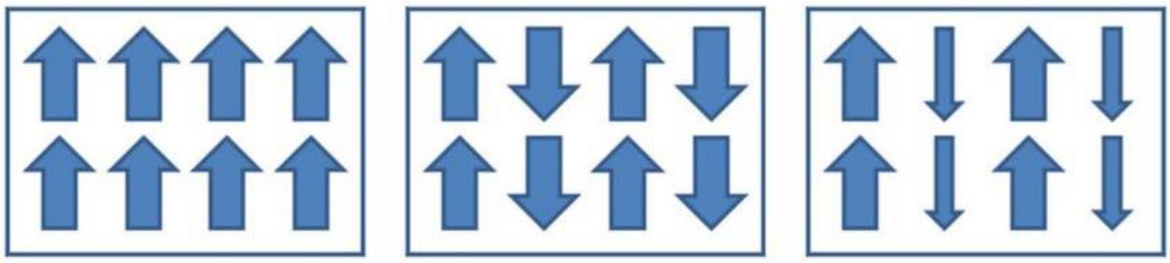

Ferromagnetism **Anti-ferromagnetism** **Ferrimagnetism**

Figure 1.3: Magnetic ordering in materials: Ferro-, Antiferro-, and Ferrimagnetism

1.5.Magnetic Hysteresis Cycle

The magnetization response of a ferrimagnetic material to an applied magnetic field H exhibits characteristic hysteresis behavior, as shown in the hysteresis loop in **Figure1.4**.

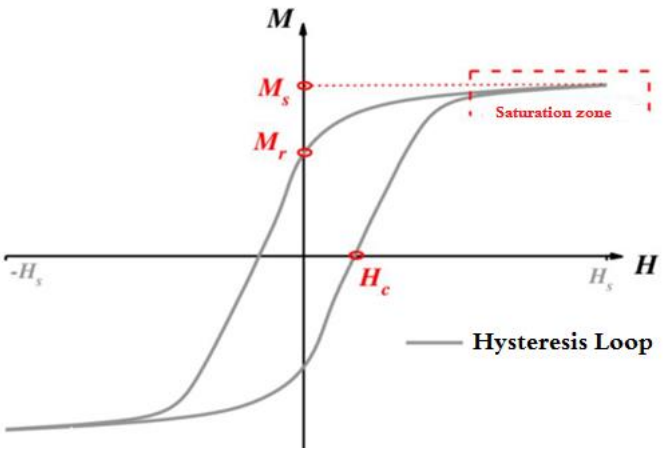

Figure1.4: Magnetic Hysteresis Cycle

At zero applied field, a residual magnetization Mr (remanence) persists. To reduce and eliminate this magnetization, the applied field must be reversed until reaching a critical value Hc (coercive field). Both coercive field and remanent magnetization exhibit temperature dependence. Above a characteristic temperature (Curie temperature, Tc), the hysteresis loop collapses and the material transitions to paramagnetic behavior [53]. The hysteresis loop of ferrimagnetic materials typically exhibits a shape similar to that of ferromagnetic systems, though with distinct Mr (remanence) and Hc (coercivity) values determined by the material's specific composition and crystal structure. The loop width may vary significantly, reflecting differences in the strength and nature of internal magnetic exchange interactions.

Magnetic Domains: The magnetic properties of ferrite particles, even at fixed composition, exhibit strong grain-size dependence. For crystallites exceeding ~1μm in size, they typically contain multiple magnetic domains separated by Bloch walls. Each domain maintains a permanent magnetic moment determined by the crystallographic orientation of the structure. Magnetization reversal in such systems occurs through domain wall motion under relatively weak applied fields [54].

For grain sizes below approximately 1μm, single-domain behavior emerges. Each particle maintains a permanent magnetic moment aligned along the easy magnetization axis. In this regime, magnetization occurs via coherent rotation of ionic magnetic moments, resulting in maximized coercivity values.

1.6.Ferrimagnetism in Ferrites

The magnetic properties of spinel ferrites are best explained within Néel's theory of ferrimagnetism [55].This theory is based on the existence of magnetic ordering resulting from spin-spin interactions between metal cations. Néel postulated the existence of two magnetic sublattices with antiparallel but unequal moments. These sublattices correspond to the two crystallographic sites (tetrahedral Td and octahedral Oh) in the spinel structure. Furthermore, Néel proposed that exchange interactions occur between metal cations in Td and Oh sites via oxygen ions (superexchange). For high doping concentrations, octahedral-octahedral (Oh-Oh) interactions become dominant, driving the system toward antiferromagnetic ordering. In such cases, the atomic coupling is antiparallel with equal moment magnitudes, resulting in zero net magnetization and exhibiting very low positive susceptibility. These exchange couplings are disrupted by thermal fluctuations above a

critical temperature (Néel temperature, TN), beyond which the antiferromagnetic materials transition to paramagnetic behavior.

1.7.Crystal Field Theory

Crystal Field Theory (CFT) is a fundamental framework for analyzing the electronic structure and properties of coordination compounds. These complexes consist of a central metal ion (typically a transition metal cation), surrounded by bound molecules, or anions-collectively termed *ligands [56]*. Crystal Field Theory (CFT) postulates that a central metal ion, when surrounded by ligands in a symmetric coordination geometry (e.g., octahedral or tetrahedral), experiences an electrostatic field that lifts the degeneracy of its d-orbitals through differential stabilization and destabilization—an effect arising from the crystal-like arrangement that gives the theory its name [57].

1.7.1. Electron 3d

Transition elements possess an incomplete 3d electron shell, resulting in localized magnetic moments (**Figure 1.**). Unlike delocalized electrons, the 3d electrons of magnetic ions do not form separate energy bands due to their limited orbital overlap. However, they can significantly influence the electronic properties of valence bands through hybridization with p-states. The 3d shell splits into a fully occupied 3d↑ level and an empty or partially filled 3d↓ level, with the specific configuration depending on the transition metal ion (Mn, Fe, Co, etc.).

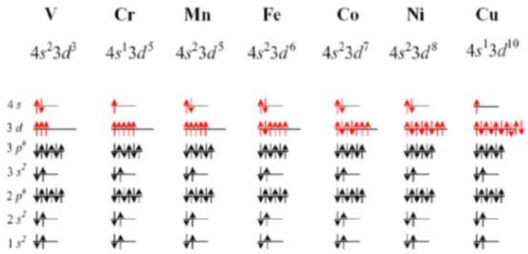

Figure 1.5 : Electronic configuration of the 3d and 4s states of transition metals

1.7.2. Degeneracy of orbitals «d»

The crystal field significantly affects the orbitals of a metal ion, destabilizing them unevenly and lifting their degeneracy. The extent of degeneracy lifting depends on the crystal field geometry, which is determined by the arrangement of ligands around the metal ion (**Figure 1**).

- **Octahedral field:** In an octahedral crystal field, six ligands surround the central metal ion, forming an octahedron. The ligands are positioned along the *x*, *y*, **and *z* axes, generating a non-uniform electric field that destabilizes the *d*-orbitals** pointing toward the ligands (antibonding orbitals) while stabilizing those directed between the ligands (bonding orbitals).**The d-orbitals split intotwo groups:**

- ✓ $t_{2g}\ orbitals$: $3d_{xy}, 3d_{y}z, 3d_{x}z$ (stabilized).
- ✓ $e_g\ orbitals$: $d\_z^2, d_x{}^2 - {}_y{}^2$ (destabilized).

The energy separation between the t2g and e_g orbitals is termed the crystal field splitting parameter (Δ_o).

- **(b) Tetrahedral field:** In a tetrahedral crystal field, four ligands surround the central metal ion in a tetrahedral arrangement. The ligands are positioned at equal angular intervals, generating an electric field that is less anisotropic than in an octahedral field.**The d-orbitals split into two groups:**

- ✓ **t_2 *orbitals*:** (stabilized
- ✓ **e *orbitals*:** (destabilized)

The energy splitting between the t2 and e orbitals is smaller than the octahedral field splitting parameter (Δ_o).

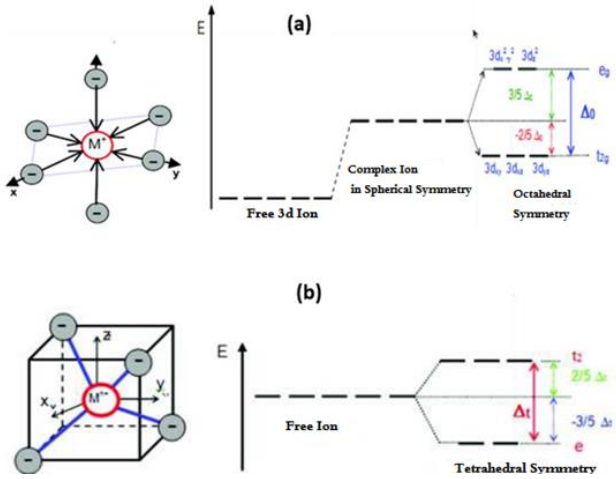

Figure 1.6: Effect of crystal field on d-orbital energy levels for (a) octahedral and (b) tetrahedral fields.

The crystal field-induced splitting of d-orbitals has significant implications for the properties and behavior of metal complexes in various physical contexts. The color of metal complexes is directly governed by this orbital splitting. Electronic transitions between the crystal field-split d-orbitals lead to the absorption or emission of visible light, giving rise to the complex's characteristic color. This phenomenon is fundamental to spectroscopic analysis and compound characterization [58].Furthermore, orbital splitting significantly influences the magnetic properties of complexes. The presence of unpaired electrons in d-orbitals, resulting from this interaction, confers magnetic behavior to the complex. The specific electron configuration determines the overall magnetic moment of the complex, which is critical for understanding its magnetic behavior.

1.8.Electrical Properties

1.8.1. Electrical conduction in spinel ferrites

The Verwey mechanism, proposed by E.J.W. Verwey in the 1950s, explains the electronic conduction at room temperature in spinel ferrites. According to this model, conduction does not result from free electron movement, but rather from polaron hopping between cations of the same element that exhibit different ionization states (differing by one unit) and occupy equivalent crystallographic sites [59].

The conduction mechanism arises not from free electron migration, but through polaron hopping between cations of the same element, which must exhibit: (i) ionization states differing by one unit, and (ii) occupation of equivalent crystallographic sites. Polarons are charge-stabilized quasiparticles consisting of an electron coupled to a localized lattice distortion [60]. This model specifically excludes electron hopping between the two crystallographic sublattices of the spinel structure (tetrahedral Td and octahedral Oh sites). Instead, it preferentially describes hopping between octahedral sites (Oh), where the intersite distance determines the most favorable electron transfer pathway.

In fact, the intersite distances observed in spinel ferrites are the following:

$$d_{OhOh} = a\frac{\sqrt{2}}{4} \quad and \quad d_{TdTd} = a\frac{\sqrt{3}}{4}\,0 \qquad \text{I-0-1}$$

Electron hopping between octahedral (O_h) sites requires the lowest energy due to the shortest intersite distance. In contrast, hopping between octahedral-tetrahedral sites or between tetrahedral sites (Td) is less probable, as it demands higher energy owing to larger intersite distances. Electrical conductivity is influenced by the cation distribution among

octahedral (Oh) and tetrahedral (Td) sites. The Verwey mechanism accounts for the relatively high electrical resistivity of spinel ferrites compared to metals.

1.8.2. Negative Temperature Coefficient (NTC) Behavior in Spinel Ferrites

NTC (Negative Temperature Coefficient) spinel ferrites exhibit distinctive properties that make them particularly suitable for various technological applications. The temperature coefficient (α) of NTC spinel ferrites is typically negative, indicating that their resistivity decreases with increasing temperature [61],making these materials highly sensitive to thermal variations.Furthermore, these ferrites exhibit high sensitivity factor (B) values, indicating a strong resistivity variation over a given temperature range, which enables enhanced accuracy in temperature measurement and control. In addition to their exceptional sensitivity, NTC spinel ferrites are also recognized for their chemical and mechanical stability, making them suitable for operation in harsh environments. This combination of thermal sensitivity and robustness establishes NTC spinel ferrites as crucial materials for numerous industrial and technological applications where precise temperature regulation and measurement are critical [62, 63].

1.8.3. Magnetic Semiconductors

Magnetic semiconductors represent a remarkable class of materials that simultaneously exhibit both semiconducting and magnetic properties. This unique combination enables concurrent control of electrical and magnetic characteristics, paving the way for transformative applications in spintronics and magnetoelectronics[64].

A cornerstone of magnetic semiconductor physics is the spin-charge coupling. In these materials, conduction electrons serve as dual carriers of both electric charge and spin magnetic moment. This dual nature establishes a reciprocal relationship between the system's magnetic state and its electronic transport properties.The Goodenough model [65] describes how magnetic ordering influences electronic conduction in magnetic semiconductors. According to this framework, charge transfer of a conduction electron from a donor site to an acceptor site is more probable when the spins of the 3d electrons at both donor and acceptor cations are parallel.

The transfer energy depends on the $\cos(\theta/2)$ factor, where θ represents the angle between the 3d electron spins of two adjacent conduction sites. This factor determines the electron transfer probability as a function of spin alignment. Charge transport is more

favorable when spins are parallel ($\theta = 0$) compared to antiparallel configurations ($\theta = \pi$). In ferromagnetic semiconductors with aligned spins, resistivity remains relatively low. Conversely, antiferromagnetic semiconductors exhibit higher resistivity due to enhanced charge carrier localization resulting from antiparallel spin ordering.

1.9.Applications and Technology

Spinel ferrites exhibit remarkable magnetic and dielectric properties that make them attractive for various technological applications. Key potential uses include:

1.9.1. Telecommunications

Ferrites play a critical role in telecommunications [66], particularly in microwave filters, circulators, and isolators, owing to their unique physical properties [67].In microwave filters, ferrites are incorporated into resonators or transmission lines where their magnetic permeability exhibits frequency-dependent behavior, enabling precise control of filter bandwidths and enhanced signal selectivity. The application of an external magnetic field modulates the ferrites' magnetic properties, facilitating dynamic filter tuning.

In circulators - passive devices that route electromagnetic signals through a port network - ferrites utilize the gyromagnetic effect. Under an applied static magnetic field, electron magnetic moments in the ferrites undergo precession, inducing electromagnetic wave rotation. This rotational behavior governs signal directionality, ensuring unidirectional circulation while preventing undesirable feedback.

Isolators safeguard sensitive components from signal reflections by permitting unidirectional signal transmission. Similar to circulators, isolators exploit the gyromagnetic properties of ferrites. An applied magnetic field induces non-reciprocal rotation of electromagnetic waves, enabling forward-propagating waves to pass with minimal insertion loss while strongly attenuating reflected waves in the reverse direction. This non-reciprocal characteristic is critical for preventing interference and signal reflections in communication systems.

1.9.2. Radar and Electronic Warfare Systems

Ferrites play a critical role in radar and electronic warfare systems by enhancing radar performance through improved sensitivity and reduced interference. Their electromagnetic

wave absorption properties enable the development of efficient wave absorbers, thereby improving radar signal clarity and detection accuracy [68].

Furthermore, ferrites can be employed for electronic countermeasures by disrupting adversarial signals through their unique magnetoelectronic properties. By exploiting the gyromagnetic effect under an applied static magnetic field, ferrites enable precise electromagnetic signal manipulation, thereby enhancing the effectiveness of jamming operations [69].

1.9.3. Consumer Electronics

The miniaturization potential and low-loss characteristics of ferrites make them promising candidates for consumer electronics applications, including smartphones, tablets, and laptops. Microwave filters and antennas fabricated from these materials can enhance device connectivity and performance. Their ability to mitigate electromagnetic interference and improve signal transmission efficiency contributes to superior reception quality and more reliable wireless communication. Integration of ferrites in electronic components enables compact device designs while maintaining high performance standards, addressing the evolving demands of modern technology [70].

1.9.4. Electric and Hybrid Vehicles

Ferrites have critical applications in power converters and filters for electric and hybrid vehicles. These components enable efficient conversion of battery-stored electrical energy into usable motor power, thereby optimizing vehicle performance. Furthermore, ferrites play a pivotal role in electromagnetic interference (EMI) suppression, enhancing the reliability and safety of onboard electronic systems. Their high-current handling capacity and energy loss minimization properties establish ferrites as essential components for improving the efficiency and durability of electric and hybrid vehicles [71].

1.9.5. Renewable Energy Systems

Ferrites can be utilized in power converters and filters for renewable energy systems, including wind turbines and solar panels. These components enable efficient conversion of renewable energy into grid-compatible electricity. Their high magnetic permeability and low energy loss characteristics are critical for optimizing power conversion efficiency and

mitigating electromagnetic interference (EMI), thereby enhancing overall system performance in renewable energy applications [72].

1.9.6. Medical Imaging

In medical imaging, the magnetic properties of ferrites make them valuable for magnetic resonance imaging (MRI). Ferrite nanoparticles can serve as contrast agents, enhancing MRI resolution and sensitivity. Their magnetic moments induce localized magnetic field perturbations, which improve image contrast and enable more accurate diagnosis of various pathologies [73].

1.9.7. Magnetic Hyperthermia

Ferrites also demonstrate potential for magnetic hyperthermia applications, a cancer treatment modality that utilizes alternating magnetic fields for localized tumor heating. When ferrite nanoparticles are delivered to tumor sites, exposure to external alternating magnetic fields induces localized heating through Néel relaxation, enabling precise thermal ablation of malignant cells while minimizing damage to healthy tissue [74].

1.9.8. Catalysis

The catalytic properties of ferrites make them valuable for diverse chemical processes. These materials serve as effective catalysts for pollutant degradation [75], chemical synthesis, and energy conversion. Their crystalline structure and redox-active surface sites enable efficient catalytic activity through enhanced chemical interactions [76].

Ferrite research continues to advance dynamically, with novel applications continuously emerging. The unique multifunctional properties of these materials demonstrate significant potential for diverse technological applications, thereby driving progress across multiple scientific disciplines and enabling improvements in everyday technologies.

CHAPTER II:

DENSITY FUNCTIONAL THEORY AND FULL-POTENTIAL LINEARIZED AUGMENTED PLANE WAVES APPROXIMATION

2.1.Introduction

Materials science encompasses the investigation of the properties, structures, and applications of materials across diverse technological and industrial fields. A fundamental aspect of this discipline involves understanding the electronic band structures of materials. Various computational and experimental **techniques** have been developed to analyze these structures. Depending on the nature of the required information, these methods can be classified into three major categories:

- Empirical methods rely primarily on experimental **data** to derive material properties and behaviors.
- Semi-empirical methods integrate experimental data with fundamental theoretical models, offering a balanced approach between computational efficiency and accuracy.
- **Ab initio methods**, which rely solely on fundamental data.

Ab initio methods are theoretical approaches based on fundamental quantum mechanical principles to model atomic and molecular behavior. Unlike empirical methods, they do not rely on experimental input but instead solve the Schrödinger equation to accurately predict electronic and structural properties of materials.

2.2.Schrödinger Equation

The **time-dependent Schrödinger equation (TDSE)** serves as the fundamental starting point for studying the electronic properties of materials from a theoretical perspective. This first-principles approach describes the quantum mechanical evolution of a many-body system under time-varying potentials, providing access to dynamic electronic behavior, excited states, and optical responses.

Mathematical Formulation:

$$H\psi(\{r_i\},\{R_I\},t)=i\hbar\frac{\partial}{\partial t}\psi(\{r_i\},\{R_I\},t) \quad (2\text{-}1)$$

The system is described using a many-particle wave function, $(\{r_i\},\{R_I\},t)$, where the set $\{r_i\}$ contains variables representing the positions of the electrons, and the set $\{R_I\}$ corresponds to the positions of the nuclei. The Hamiltonian of the system, denoted as H,

governs its dynamics. Due to the large number of degrees of freedom inherent in this wave function, the system's ground state can be obtained by solving the time-independent Schrödinger equation (stationary state) [77].

$$H\psi(\{r_i\},\{R_I\})=E\psi(\{r_i\},\{R_I\}) \qquad \text{II -2}$$

Where E represents the energy of the ground state described by the eigenfunction ψ. Typically, the Hamiltonian operator is expressed as:

$$H= T_E\,(r)+ T_N\,(R)+ V_{ee}\,(r)+ V_{NN}\,(R)+ V_{Ne}\,(r,R) \qquad \text{II -3}$$

Where T_e and T_N are the kinetic energy operators for electrons and nuclei, respectively, V_{ee} and V_{NN} are the operators representing the repulsive potential energy between electrons and between nuclei, and V_{Ne} is the operator for the attractive potential energy between nuclei and electrons. These operators can be expressed (in electrostatic units where $4\pi\varepsilon_0$=1) as:

$$T(r)= -\frac{\hbar}{2m}\sum_i^N \nabla_i^2 \quad \text{and} \quad TN(R)= -\frac{\hbar}{2m}\sum_I^A \nabla_I^2 \qquad \text{II-4}$$

$$Ve(r)=\sum_{i<j}\frac{e^2}{|r_i-r_j|} \quad \text{and} \quad V_{NN}(R)= \sum_{I<J}\frac{Z_I Z_J e^2}{|R_I-R_J|} \qquad \text{II-5}$$

$$V_{Ne}(r,R)= \sum_{i,I}\frac{Z_I e^2}{|r_i-R_I|} \qquad \text{II-6}$$

Where $\hbar = h/2\pi$ (h being the Planck constant), m is the electron mass, M is the nucleus mass, and Z is its charge. However, obtaining its exact solution is often challenging, particularly for complex systems. For this reason, numerous approximate methods have been developed to solve the Schrödinger equation.

2.3.Born-Oppenheimer (Adiabatic) Approximation

The Born-Oppenheimer (BO) approximation [78] relies on the fact that the mass of any atomic nucleus is significantly larger than that of an electron. As a result, nuclear motion can be neglected relative to electronic motion—meaning the nuclei are treated as fixed. In other words, the BO approximation decouples electronic and nuclear dynamics by separating the system into two coupled subsystems: one for the electrons and another for the nuclei:

$$\psi \approx \psi_{BO}=\psi_{élec}\times\psi_{noyaux} \qquad \textit{II-7}$$

The electronic configuration can thus be considered fully relaxed to its ground state for every ionic position during their motion. Consequently, the nuclear kinetic energy is neglected, and the nucleus-nucleus potential energy reduces to a constant. This approximation

transforms the original problem—requiring solution of the Schrödinger equation for an *N*-electron system under the influence of the nuclear potential—into a simplified framework.

In this regime, the Hamiltonian retains only one-electron (T_e and V_{eN}) and two-electron (Vee) contributions. We may therefore define a new electronic Hamiltonian, H_e, given by:

$$H_e = T_e + V_{e-e} + V_{eN} \quad \text{II-8}$$

Or

$$H_e = \frac{-\hbar^2}{2m_i}\sum_i \nabla_i^2 + \frac{1}{2}\sum_{i,j}\frac{e^2}{|r_i - r_j|} + \sum_{i,j}\frac{e^2}{|r_i - R_a|} \quad \text{II-9}$$

The Schrödinger equation can then be written as:

$$\left[\frac{-\hbar^2}{2m_i}\sum_i \nabla_i^2 + \frac{1}{2}\sum_{i,j}\frac{e^2}{|r_i - r_j|} + \sum_{i,j}\frac{e^2}{|r_i - R_a|}\right]\psi_e = E_e\psi_e \quad \text{II-10}$$

The Born-Oppenheimer approximation is termed "adiabatic" because it effectively decouples the electronic problem from lattice vibrations. While the nuclear kinetic energy (T_n) and nucleus-nucleus potential (V_{nn}) can be subsequently reintroduced to address lattice vibrations (phonons), **this** approach fundamentally assumes no energy exchange occurs between the electronic system and vibrational modes.

The Schrödinger equation solution can thus be restricted to the electronic problem. For notational simplicity, all quantities will be implicitly considered as electronic properties unless otherwise specified. At this stage, the wavefunction of an electron system in a nuclear potential field appears primarily useful for determining the system's energy. While the wavefunction itself lacks direct physical meaning, its squared modulus is directly related to the electron density distribution.

The Born-Oppenheimer approximation represents a fundamental simplification that enables the treatment of a solid as a system of interacting electrons moving within the static potential field of fixed nuclei. However, solving the Schrödinger equation remains highly complex in most cases, typically requiring additional approximations based on mean-field theories. In such approaches, electrons are treated as independent particles, with the Hartree approximation being one of the most prominent examples [79].

2.4.Free-Electron Approximation (Hartree)

The approach developed by Hartree [79, 80] models the Coulomb interaction through an effective Hartree potential V_{Hartree}, which acts on each electron and represents the mean-field effect of all other electrons. This potential is defined by:

$$V_{\text{Hartree}}=\sum_j \int dr'_{(r)}\, \psi^* \qquad \text{II-11}$$

And to express the wave function as a product of single-electron wave functions.

$$(r) = \prod_{i=1}^{Nél} \psi_i\,(r) \qquad \text{II-12}$$

Each single-electron wavefunction is then governed by:

$$H_{eff}\psi(r)= \left[-\frac{1}{2}\nabla^2 V_{\text{Hartree}}(r) + V_{\text{ext}}\right]\psi i\ (\text{r}) = \varepsilon_i \psi_i(r) \qquad \text{II-13}$$

Since the Hartree potential depends on orbital i, Equation (II.13) must be solved self-consistently. The ground state is obtained by filling the first n electronic energy levels. This approximation relies on the free-electron hypothesis, which effectively neglects both electron-electron interactions and spin states. This simplification has two significant consequences:

- The total Coulomb repulsion $V_{e\text{-}e}$ of the electronic system is **o**verestimated (since the initial Hamiltonian represents only a mean-field approximation).
- The Pauli exclusion principle is not accounted for (electrons are not treated as ermions).

Since this second limitation is more severe than the first, the Hartree-Fock approximation [81] was developed to incorporate electron spin effects in the solution of the Schrödinger equation.

2.5.Hartree-Fock Approximation

In this approach, first implemented in 1930 [82], no approximation is made to the Hamiltonian. Instead, the wave function is assumed to be expressible as a Slater determinant constructed from n single-electron wave functions ψ_i. This formulation explicitly accounts for the Pauli exclusion principle (thereby incorporating electron spin effects in the solution of the Schrödinger equation):

$$\psi_{el}(r) = \frac{1}{\sqrt{n!}} \begin{vmatrix} \psi_1(r_1) & .. & \psi_n(r_1) \\ : & :: & : \\ \psi_1(r_n) & .. & \psi_n(r_n) \end{vmatrix} \qquad \text{II-14}$$

Given the normalization of the wave function, the energy expression takes the form:

$$E_{HF}(r) = \langle \psi_{el}(\{r\}) | H | \psi_{el}(\{r\}) \rangle \quad \text{With}$$

$$\begin{cases} \int dr \psi_i^*(r) \left[-\frac{1}{2}\nabla^2 + V_{\text{el-noy}} + V_{\text{ext}} \right] \psi_i(r) \\ J_{ij} = \iint dr dr' \psi_i(r) \psi_i^*(r) \frac{1}{|r'-r|} \psi_j^*(r') \psi_j(r') \\ K_{ij} = \iint dr dr' \, \psi_i^*(r) \psi_j(r) \frac{1}{|r'-r|} \psi_i(r') \psi_j^*(r') \delta(\sigma_i - \sigma_j) \end{cases} \qquad \text{II-15}$$

The term J_{ij} represents the Coulomb integral, already present in the Hartree approach, while K_{ij} denotes the exchange integral (or Fock term), which arises from the wavefunction antisymmetry requirement. To determine the orbitals (r), we employ the Rayleigh-Ritz variational principle to minimize the Hartree-Fock energy$E_{HF}(r)$, subject to wavefunction normalization constraints

$$\delta \left(E_{HF}(r) - \sum_{i,j} \lambda_{i,j} (\langle \psi_i | \psi_j \rangle - \delta_{i,j}) \right) = 0 \qquad \text{II-16}$$

Through a unitary transformation, the matrix of Lagrange multipliers $\lambda_{i,j}$ can be diagonalized, yielding the single-electron Fock equations:

$$\left[T_{el} + V_{el-nu} + V_{Hartree} + V_{fock}(\{\psi(r)\}) \right] \psi_i(r) = \varepsilon_i \psi_i(r) \qquad \text{With}$$

$$\begin{cases} V_{Hartree} = \sum j \int dr' \psi_j(r) \psi_j(r^*) \frac{1}{|r'-r|} \\ V_{fock} = \left[\sum j \int dr' \psi_j(r) \psi_j(r^*) \frac{1}{|r'-r|} \right] \frac{\psi_j(r)}{\psi_i(r)} \delta(\sigma_i - \sigma_j) \end{cases} \qquad \text{II-17}$$

where the Lagrange parameter is identified as a single-electron energy. This system of equations is self-consistent (through both the Hartree term and the non-local Fock term).

The Hartree-Fock approximation is grounded in the variational principle, which requires minimization of the total energy. Specifically, the system's total energy is obtained by minimizing the expectation value of the Hamiltonian operator and is formally defined as a wavefunction functional:

$$E[\psi] = \frac{\int \psi^* H \psi}{\int \psi^* \psi} \qquad \text{II-18}$$

By virtue of the variational method, the selection of optimal spin-orbitals corresponds to minimizing the electronic energy (E_e). This optimized electronic wavefunction, obtained at

the lowest achievable energy, will always lie above the exact ground-state energy. The energy minimization procedure constitutes a self-consistent process subject to orbital orthonormality constraints. The variational calculation demonstrates that each wavefunction $\psi_i(r)$ must satisfy a second-order differential equation – taking the form of a single-particle Schrödinger equation – to minimize the expectation value ⟨H⟩.

$$[-\nabla^2 + (r) + (r)](r) = E_i\psi_i(r) \qquad \text{II-19}$$

The first potential term (r) in this equation derives directly from the Hamiltonian H. It represents the Coulomb interaction between the electron and all nuclei in the crystal, exhibiting the periodicity of the Bravais lattice. The second term $U_i(r)$, called the self-consistent mean potential, accounts for the Coulomb repulsion exerted on electron i by all other electrons (j≠i), with each electron j occupying its respective state ψ_j.

$$U_i(r) = \int\int\int \frac{q^2\rho_i(r')}{|r-r'|} \qquad \text{II-20}$$

In this model, the electron cloud perceived by a given electron is treated as a continuous negative charge distribution characterized by the charge density ρ(r), defined as:

$$(r) = \sum_i |\psi(r)|^2 \qquad \text{II-21}$$

The system comprises N equations of the form (II.19) (one for each electron), each distinct yet mutually coupled through the potentials U(r). In practice, an exact solution of the system remains computationally intractable without introducing additional approximations. Consequently, the equations must be solved iteratively until self-consistency of the solutions is achieved. The exchange term is defined as:

$$V_{exch} = \sum_{j\neq i}\int \frac{\psi_j^*(r')\psi(r')}{|r-r'|}\psi_j(r)dr' \qquad \text{II-21}$$

This yields the Hartree-Fock equations

$$[-\nabla^2 + w(r) + U_i(r)]\psi_i(r) - \sum_{j\neq i}\int \frac{\psi_j^*(r')\psi(r')}{|r-r'|}\psi_j(r)dr'\psi_i(r) = \varepsilon_i\psi_i(r) \qquad \text{II-23}$$

In the Hartree-Fock method, the total system energy is defined as a wavefunction functional. While this approach accounts for electron exchange effects, it neglects electron correlation - the dependence of one electron's motion on the instantaneous positions of all others. Post-Hartree-Fock methods capture only partial correlation energy and are computationally

feasible only for small systems. For larger molecules or solid-state systems, density functional theory (DFT) proves significantly more suitable.

2.6.Density Functional Theory (DFT)

Density Functional Theory (DFT) represents one of the most powerful ab initio computational methods for investigating the electronic structure of atoms, molecules, crystals, and surfaces. The initial framework was proposed by Thomas and Fermi in the 1920s [83]. A significant advancement in electronic structure theory was achieved through the formal formulation by Hohenberg and Kohn [84].

2.6.1. Fundamental Principles

Building on historical foundations, Thomas and Fermi first introduced electron density as the fundamental variable for modeling system properties. While groundbreaking, their approach proved quantitatively inadequate for describing molecular and solid-state systems. The field advanced significantly decades later through the work of Slater, Hohenberg, and Kohn, who established a rigorous theoretical framework. Their formulation definitively identified electron density—not wavefunctions—as the key determinant of ground-state properties in DFT.

This paradigm shift offers two critical benefits: (1) versatility across diverse systems, and (2) maintained accuracy with tractable computational cost. The theory's power stems from expressing many-electron energies exclusively through electron density—a size-independent quantity that avoids the exponential complexity of wave function methods.

In their formalism, they introduced an exchange-correlation functional that models the exchange-correlation hole - a critical component in quantum chemistry calculations. Subsequently, we will review: the Hohenberg-Kohn theorems, the fundamental principles of the method and the various approximation approaches for the exchange-correlation functional.

2.6.2. Hohenberg-Kohn Theorems

The theoretical framework of Density Functional Theory (DFT) is fundamentally grounded in the Hohenberg-Kohn theorems [85]. These theorems apply to an N-electron

system moving within a fixed external potential $V_{ext}(r)$ generated by nuclear charges, where the Hamiltonian takes the form:

$$H = -\frac{\hbar}{2m_e}\sum i\,\nabla_i^2 + \sum i\,V_{ext}(r_i) + \frac{1}{2}\sum i \neq j\,\frac{e^2}{|r_i - r_j|} \qquad \text{t} \qquad \text{II-24}$$

Theorem 1:

The First Hohenberg-Kohn Theorem establishes that for any interacting electron system, the ground-state electron density $\rho_0(r)$ uniquely determines (up to an additive constant) the external potential $V_{ext}(r)$ – since different spatial potentials cannot produce identical charge densities – and consequently specifies all properties of the system, as the density effectively encodes the complete many-body wavefunction and Hamiltonian.

The total energy of the ground state of an interacting electron system is a unique (albeit unknown) functional of the electron density.

Theorem 2:

Hohenberg and Kohn demonstrated that the total energy of a system can be expressed as a functional of the electron density, E= $\boldsymbol{E[\rho]}$. The minimum of this total energy corresponds to the exact ground-state density $\boldsymbol{\rho(r) = \rho_0(r)}$. Consequently, the variational principle can be readily applied to determine the ground-state energy and electron density for a given external potential. Moreover, all other ground-state properties are also functionals of this ground-state electron density.

The energy of the ground-state density, $\boldsymbol{E[\rho_0]}$, is always lower than the energy of any other trial density, $\boldsymbol{E[\rho]}$

$$E_0 = E[\rho_0] \qquad \text{II-25}$$

An extension of these properties to a spin-polarized system is feasible, provided that E is generalized as a functional of the two spin densities: $E[\rho] = E[\rho_\uparrow, \rho_\downarrow]$. In this framework, the applicability and utility of density functional theory (DFT) hinge critically on the form of the density functional $[\rho]$. While the preceding theorems establish its existence, they provide no explicit construction. Consequently, developing sufficiently accurate approximations for $E[\rho]$ becomes an essential requirement for practical computations.

2.6.3. Kohn-Sham Approach

The Kohn-Sham equations, published in 1965 [86], transformed density functional theory (DFT) into a practical tool for calculating ground-state energies of electronic systems. This approach enables the determination of exact many-body system properties through independent-particle methods. Their formulation is based on the following key concept: An interacting electron gas can be mapped exactly onto a system of non-interacting fictitious particles, described by single-particle wavefunctions $\psi_i(r)$. This auxiliary system is constructed such that its ground-state electron density - and consequently its total energy E[ρ] - matches exactly that of the original interacting electron gas.

$$H_{ks}\psi_i(r) = \left[T_e(r) + V_{eff}(r)\right]\psi_i(r) = \varepsilon_i\,\psi_i(r) \qquad \text{II-26}$$

Where $T_e(r)$ represents the kinetic energy operator of the non-interacting fictitious particles, and ε_i denotes the eigenvalue associated with the single-particle state $\psi_i(r)$. These fictitious particles experience an effective potential $V_{eff}(r)$ that can be expressed as the sum of three distinct potential terms:

$$V_{ef}(r)=V_{ext}(r)+V_H(r)+V_{XC}(r) \qquad \text{II-27}$$

Here, $V_H(r)$ represents the Hartree potential, corresponding to the classical Coulomb interaction between electrons in the electron gas, while (r) denotes the exchange-correlation potential. Both potentials can be expressed as direct functionals of the electron density $\rho(r)$:

$$V_H(r) = e^2 \int \frac{\rho(r')}{|r-r'|} d^3r' \qquad \text{II-28}$$

$$V_{XC}(r) = \frac{\delta E_{XC}[\rho]}{\rho(r)} \qquad \text{II-29}$$

The Hohenberg-Kohn theorems and the subsequent derivation of the Kohn-Sham single-particle equations are mathematically rigorous, achieved without introducing any approximations. However, the exchange-correlation functional $V_{XC}(r)$ in the Kohn-Sham equations precludes exact solutions, as its analytical form remains unknown. Practical implementation therefore requires an approximate analytical expression for the exchange-correlation energy $E_{XC}[\rho]$.

2.6.3.1.Exchange-Correlation Potential Formulation $V_{XC}(r)$

This potential constitutes the cornerstone of density functional theory, as it accounts for the exchange-correlation effects lost when replacing the true many-body wavefunction with non-interacting single-particle Kohn-Sham orbitals. It effectively compensates for the information deficit arising from this mapping between the interacting electron gas and its fictitious independent-particle counterpart.

In a real electron gas, electrons with parallel spins experience an effective repulsion due to the Pauli exclusion principle. The resulting energy reduction of the interacting electron gas, compared to a hypothetical system with only Coulomb interactions, defines the exchange energy.

The system energy can be further modified by increasing the separation distance between electrons with antiparallel spins. However, while this reduces Coulombic repulsion, it simultaneously increases the kinetic energy of the electron gas. The resulting energy difference between this correlated many-body system and the Hartree-Fock reference state defines the correlation energy, which may be expressed as:

$$V(r)=[T_e(r)-T_{e'}(r)]+[V_{int}(r)-V_H] \qquad \text{II-30}$$

Thus, $V_{XC}(r)$ represents the difference in both kinetic and internal energy between the real interacting electron gas and the fictitious Kohn-Sham system, where electron-electron interactions are reduced to the classical Hartree term. Despite the long-range nature of Coulomb interactions, the exchange-correlation potential $V_{XC}(r)$ constitutes a local physical quantity, reflecting the short-range nature of many-body quantum effects.

Electron-electron interactions give rise to three fundamental quantum mechanical effects: exchange, originating from the Pauli Exclusion Principle, which enforces zero probability density for same-spin electrons at identical positions (Fermi hole). A direct consequence of the wave function anti-symmetry requirement under electron coordinate exchange; dynamic correlation, representing the instantaneous Coulombic repulsion between electrons; and non-dynamic (static) correlation, arising from near-degeneracy effects in molecular systems.

The exchange effect is fundamentally spin-dependent and independent of electronic charge, being inherently accounted for in Hartree-Fock theory [5] through the antisymmetry requirement of the Slater determinant [87] representing the many-electron wavefunction.

While Hartree-Fock includes exchange exactly, it neglects electron correlation - a charge-dependent effect arising from Coulombic repulsion $\frac{1}{r-r_0}$ between electrons. This correlation manifests primarily through dynamic adjustments in electron motion to avoid one another, with particularly significant effects in core electron regions due to their high local density. The third effect arises from the independent-particle formulation of electronic wave functions, specifically the self-interaction correction required for proper electron pair counting. Additionally, the exchange-correlation functional must account for the kinetic energy difference between the non-interacting reference system and the real interacting system. Consequently, accurate determination of both the exchange-correlation energy and potential necessitates carefully constructed approximations that address these fundamental challenges.

The accuracy of the Kohn-Sham approach hinges entirely on the ability to compute the exchange-correlation potential $V_{XC}(r)$ as precisely as possible. However, since its exact analytical form remains unknown for general systems, solving the Kohn-Sham equations presents a fundamental challenge. To address this, various approximate exchange-correlation functionals have been developed, enabling practical implementations of density functional theory while balancing computational efficiency with physical accuracy.

2.6.3.2.Local Density Approximation (LDA)

In their seminal work, Kohn and Sham proposed treating solids as a homogeneous electron gas, where exchange-correlation effects can be reasonably approximated as local phenomena. This foundational assumption led to the Local Density Approximation (LDA), which expresses the exchange-correlation energy as:

$$E_{XC}^{LDA} = \int \rho(r)\varepsilon_{XC}^{hom}[\rho(r)]d^3r \equiv \int \rho(r)\left\{\varepsilon_X^{hom}[\rho(r)] + \varepsilon_C^{hom}[\rho(r)]\right\}d^3 \quad \text{II-31}$$

Here, $\varepsilon_{xc}([\rho], r)$ represents the exchange-correlation energy per particle of a homogeneous electron gas with local density $\rho(r)$. While this approximation neglects non-local density variations, it provides a remarkably robust starting point for quantitative calculations in solid state systems.

To properly account for spin polarization effects, the LDA framework was subsequently generalized to the Local Spin Density Approximation (LSDA). This extension modifies the density functional by explicitly incorporating both spin states (↑ and ↓), where the exchange-correlation energy becomes dependent on the spin densities $\rho_{\uparrow}$ (**r**) and $\rho_{\downarrow}$ (**r**) rather than just the total electron density $\rho(r)$.

$$E_{XC}^{LDA} = \int \rho(r)\varepsilon_{XC}^{hom}[\rho_{\uparrow}, \rho_{\downarrow}]d^3r \qquad \text{II-32}$$

The homogeneous exchange potential ε_X^{hom} [n(r)] admits an exact analytical expression via the exchange energy functional originally formulated by Dirac [11]. This term, widely known as the "Dirac exchange," is an exact and well-established contribution to the exchange-correlation energy in density functional theory.

$$\varepsilon_x(\rho) = -\frac{3}{4}\left(\frac{3}{\pi}\rho(r)\right)^{1/3} \quad with \quad \rho = \left(\frac{4\pi r^3}{3}\right)^{-1} \quad and \quad r = \left(\frac{3}{4\pi n}\right)^{1/3}\frac{1}{a_0} \qquad \text{II-33}$$

The **correlation** component, being more complex to evaluate, has been treated through various approaches. High-accuracy quantum Monte Carlo calculations performed by Ceperley and Alder (CA) [88] provided benchmark results for the homogeneous electron gas, which were subsequently parameterized into practical functional forms by various authors [89]. While LDA demonstrates remarkable performance for many systems, its limitations become apparent when describing strongly delocalized electronic systems. These shortcomings arise fundamentally from the approximation's inability to account for local electron density inhomogeneities. Systematic errors manifest in several ways, including: underestimation of bond lengths in crystalline systems, and overestimation of cohesive energies. These deficiencies can be significantly mitigated by incorporating density gradient corrections through the Generalized Gradient Approximation (GGA), which accounts for spatial variations in the electron density distribution.

2.6.3.3.Generalized Gradient Approximation (GGA)

The success of the local density approximation (LDA) spurred the development of various generalized gradient **approximations** (GGAs), leading to significant improvements and better adaptability to the systems under study. This approximation involves treating the exchange-correlation term not merely as a function of the density alone, but as a local functional doubly parameterized by both the density (ρ) and the magnitude of its gradient

$|\nabla_\rho|$. The essence of the generalized gradient approximation (GGA) lies in the selection of these functional forms, enabling better adaptability to large density variations while preserving the desired physical properties.

In its general form, the energy can be written as [90]:

$$E_{XC}^{GGA}[\rho] = \int \rho(r)\varepsilon_{XC}^{hom}[\rho(r)\varepsilon_X^{hom}]d^3r \equiv \int \rho(r)\varepsilon_x^{hom}(\rho)F_{XC}[\rho|\nabla_n|,\dots]d^3r \qquad \text{II-34}$$

Here, ε_X^{hom} represents the exchange energy of a non-**polarized** system with electron density $\rho(r)$.

As previously discussed, the exchange and correlation terms can be treated separately. The GGA (Generalized Gradient Approximation) has proven highly successful across numerous applications, delivering superior accuracy compared to LDA (Local Density Approximation)—particularly for magnetic systems and systems exhibiting strong electron density variations.

2.6.3.4. DFT+U Approximation

The DFT+U method provides a correction scheme for the self-interaction error by introducing an effective local term (U_{eff}) applied to d- or f-type orbitals. The conceptual foundation of DFT+U originates from the phenomenological Hubbard model, where the two-electron repulsion - similar to the Hartree-Fock (HF) approach - is decomposed into two distinct terms: a Coulombic term (U) and an exchange term (J). The first (diagonal) term represents the repulsion energy between two electrons occupying the same site i, while the second (off-**diagonal**) term corresponds to the exchange energy between spins on sites i and j. The magnitude of J determines whether the interaction between these states is ferromagnetic or antiferromagnetic in nature. In the DFT+U implementation proposed by Dudarev [91], both Hubbard model parameters U and J are incorporated through a single effective parameter ($U_{eff} = U - J$). The Ueff correction introduced in DFT+U, as compared to conventional DFT, effectively reduces the local one-electron potential for the targeted orbitals. This potential modification induces orbital relocalization (particularly in d- or f-orbitals), which directly impacts the spin states of transition metals (d-block elements) or f-electron systems. The DFT+U method has thus become essential for studying electronic structures of periodic solids containing transition metals (d-block elements) or f-elements,

offering superior computational efficiency compared to hybrid DFT/HF approaches. In the LDA+U or GGA+U formalism, a local correction is selectively applied only to the d-orbitals (in our case of interest) through the introduction of a Hubbard-type term: $\frac{1}{2}\sum_{i\neq j} n_i n_j$. A general expression for this approach can be formulated as follows:

$$E_{DFT+U} = E_{DFT} + E_U - E_{dc} \qquad \text{II-35}$$

Where E_U represents the Hubbard correction and E_{dc} denotes the double-counting energy.

This equation demonstrates that the system energy in DFT+U is computed by adding a corrective term to the base energy obtained from either LSDA or GGA approximations. This correction term better accounts for electronic correlations and effectively replaces the inadequately calculated portion of the energy in the LSDA or GGA framework. As shown in equation (II.35), the double-counting energy (E_{dc}) must be subtracted to avoid redundant inclusion of equivalent interaction terms.

2.6.3.5. Tran-Blaha Modified Becke-Johnson Potential Approximation (TB-mBJ)

Tran and Blaha [92] proposed an alternative approach to improve the band gap energy calculated with density functional theory (DFT) by modifying the Becke-Johnson potential, as expressed by the following relation:

$$U_{X,\sigma}^{BJ}(r) = U_{X,\sigma}^{BR}(r) + \frac{1}{\pi}\sqrt{\frac{5}{6}}\sqrt{\frac{t_\sigma(r)}{\rho_\sigma(r)}} \qquad \text{II-36}$$

Here $\rho_\sigma = \sum_{i=1}^{N_\sigma} |\psi_i, \sigma|^2$ is the electron density; $t_\sigma = \left(\frac{1}{2}\right)\sum_{i=1}^{N_\sigma} \nabla^* \psi_{i,\sigma} \nabla^* \psi_{i,\sigma}$ is the kinetic energy density, and :

$$U_{X,\sigma}^{BR}(r) = -\frac{1}{b_\sigma(r)}\left[1 - e^{-X_\sigma(r)} - \frac{1}{2}X_\sigma(r)e^{-X_\sigma(r)}\right] \qquad \text{II-37}$$

It is the Becke-Roussel (BR) exchange potential, which was proposed to model the Coulomb potential created by the exchange hole. In equation (II.36), X_σ is determined from a nonlinear relation involving ρ_σ, $\nabla\rho_\sigma$, $\nabla^2\rho_\sigma$, and t_σ. b_σ is computed as:

$$b_\sigma = [X_\sigma^3 e^{-X_\sigma}/(8\pi\rho_\sigma)]^{1/3} \qquad \text{II-38}$$

Tran and Blaha introduced an empirical parameter 'c' to adjust the relative weights of the two terms in the BJ potential, resulting in the modified TB-mBJ potential expressed as:

$$U_{X,\sigma}^{TB-mBJ}(r) = cu_{X,\sigma}^{BR}(r) + (3c-2)\frac{1}{\pi}\sqrt{\frac{5}{6}\sqrt{\frac{t_\sigma(r)}{\rho_\sigma(r)}}} \quad \text{II-39}$$

A prescription for calculating 'c' is provided in reference [93] as:

$$c = \alpha + \beta\left[\frac{1}{V_{cell}}\int\frac{|\nabla\rho(r')|}{\rho(r')}d^3r'\right] \quad \text{II-40}$$

where V_{cell} denotes the unit cell volume, and α and β are free parameters with values α = -0.012 and β = 1.023 $Bohr^{1/2}$, as determined by fitting to experimental results.

2.6.4. Solution of the Kohn-Sham Equations

DFT-based methods are categorized according to the representations used for the electron density, potential, and particularly the Kohn-Sham orbitals. The representation choice is optimized to minimize computational cost while maintaining accuracy. The Kohn-Sham orbitals are given by:

$$\psi_i(\vec{r}) = \sum C_{ij}\phi_j(\vec{r}) \quad \text{II-41}$$

where $\phi_j(\vec{r})$ are the basis functions and C_{ij} the expansion coefficients. Solving the Kohn-Sham equations requires determining the coefficients C_{ij} for the occupied orbitals that minimize the total energy. To simplify computations, the Kohn-Sham equations are solved at high-symmetry points within the first Brillouin zone. This procedure is illustrated in the flowchart of Figure 02.1. The calculation employs a self-consistent iterative cycle: starting with an initial charge density ρ_{in}, the secular equation is diagonalized:

$$(H - \varepsilon_i S)C_i = 0 \quad \text{II-42}$$

Here, **H** is the Hamiltonian matrix and **S** the overlap matrix. The new output charge density ρ_{out} is then reconstructed from the eigenvectors of this secular equation, using the total charge density obtained by summing over all occupied orbitals. If the results do not converge, the input and output densities (ρ_{in} and ρ_{out}) are mixed as follows:

$$\rho_{in}^{i+1} = (1-\alpha)\rho_{in}^{i} + \alpha\rho_{out}^{i} \quad \text{II-43}$$

Here, i^{th} denotes the iteration number and $\boldsymbol{\alpha}$ is a mixing parameter. The iterative procedure is repeated until convergence is achieved.

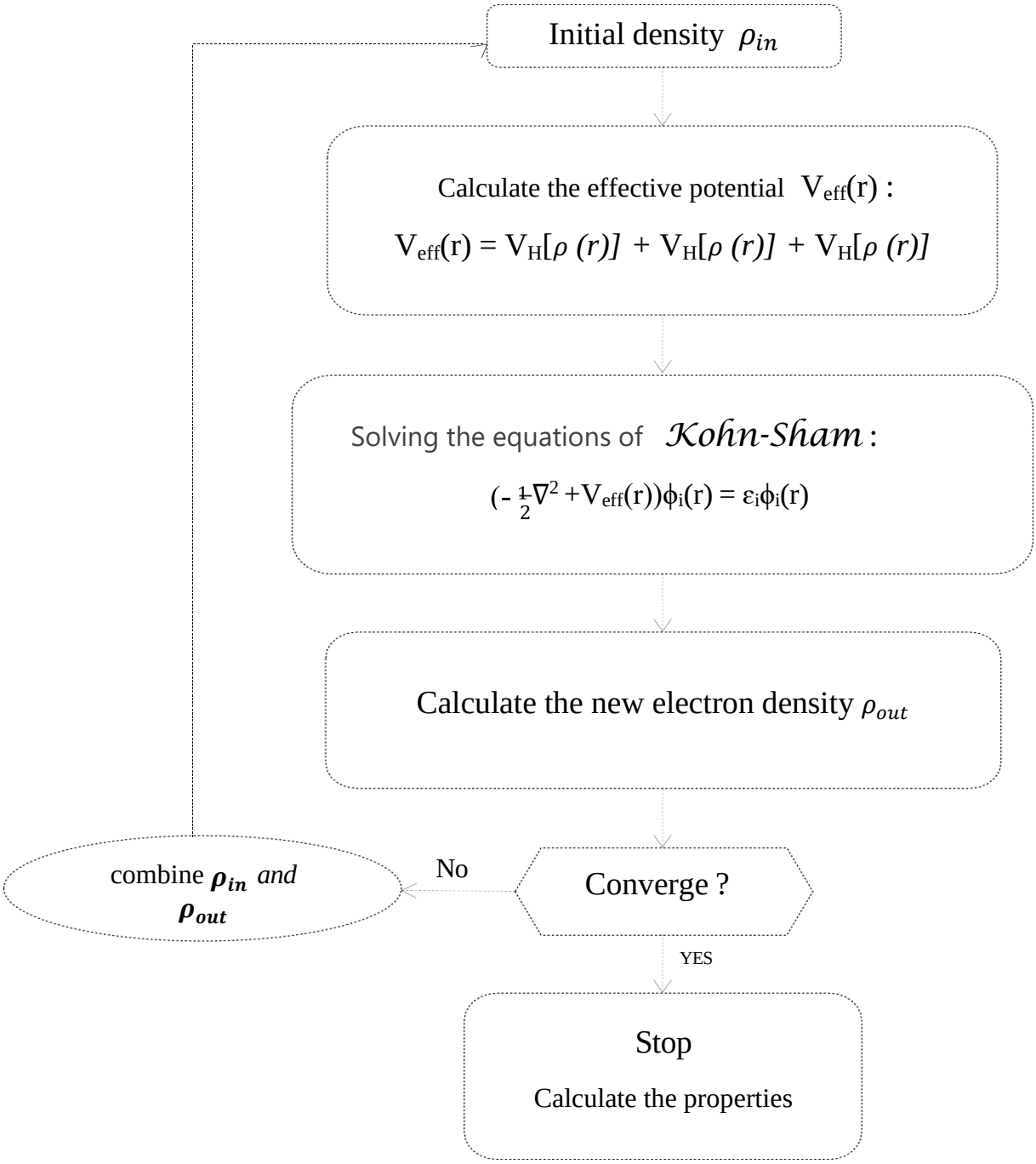

Figure 02.1 : Schematic Flow Diagram of the Kohn–Sham Density Functional Theory Approach

Density functional theory (DFT) encompasses multiple computational approaches, which are distinguished by their representations of the electronic potential, charge density,

and basis sets for wave function expansion. A key differentiation among these methods lies in their treatment of electronic states—specifically, the separation into strongly bound core states and valence states. All implementations, irrespective of their specific formalism, handle these two classes of states independently.

2.7.1. Concept of the FP-LAPW Method

The Full Potential Linearized Augmented Plane Wave (FP-LAPW) method [94, 95] ensures the continuity of the potential at the muffin-tin (MT) sphere boundary and expands it in the following form:

$$V(r)=\begin{cases}\sum_{lm} V_{lm}(r)Y_{lm}(r) \\ \sum_{k} V_{k}e^{ikr}\end{cases} \quad \text{II-44}$$

Similarly, the charge density is expanded as:

$$\rho(R) = \begin{cases}\sum_{K} \rho_{K}e^{ikr} & r > R_a \\ \sum_{k} \rho_{lm}(r)Y_{lm}(r) & r < R_a\end{cases} \quad \text{II-45}$$

The FP-LAPW (Full Potential Linearized Augmented Plane Wave) method is based on the self-consistent solution of the Kohn-Sham equations within two distinct regions of the unit cell: non-overlapping atomic spheres (muffin-tin spheres) with radii R_a, and the interstitial region between these spheres. Within the FP-LAPW framework, both the potential V(r) and charge density ρ(r) are represented by: radial/angular basis functions inside muffin-tin spheres (Region I), and plane waves in the interstitial region (Region II). This full-potential treatment explicitly includes non-spherical components, enabling accurate electronic structure calculations. All computations were carried out using the WIEN2k implementation of this method, developed by Blaha and Schwarz [96].

2.8. WIEN2k Code

The WIEN2k code is a computational package developed by Blaha, Schwarz, and collaborators **[94]** for first-principles electronic structure calculations within the density functional theory (DFT) framework**.** The WIEN2k code (originally named after the Vienna Institute for Electronic Structure Calculations**)** was developed at the Institute of Materials Chemistry, Vienna University of Technology (TU Wien)**, by** Peter Blaha and

collaborators **[95].** WIEN2k is structured as a modular computational suite, consisting **of** independent subprograms interconnected through CSHLL script-based workflows.

The determination of material properties using WIEN2k involves three principal computational phases: (1) system initialization (structural and basis setup), (2) self-consistent charge density calculation (achieving electronic convergence), and (3) physical property computation (post-processing analysis). The computational workflow for phases (1) and (2) is schematically presented in Figure II-3.

2.8.1. Initialization

The initialization phase employs five sequentially executed programs to generate all required input data for the self-consistent field calculation. The key program, NN (Nearest Neighbors), performs critical geometric analysis by: identifying first-neighbor atoms for each crystallographically unique atomic site, determining their precise spatial coordinates and interatomic distances, and calculating optimized muffin-tin radii (RMT) for each atomic species. This geometric preprocessing establishes essential parameters for accurate electronic structure calculations in both the atomic sphere and interstitial regions. The LSTART program performs relativistic atomic orbital calculations for all constituent species and generates the atomic charge densities required by DSTART. This computation requires two key input parameters: the exchange-correlation functional type and the energy cutoff distinguishing core from valence states. This program performs two critical validation functions: it verifies the complete spatial localization of core states within their respective muffin-tin spheres prior to self-consistent density calculations, and establishes the computational treatment methodology for valence states.

The SYMMETRY program performs comprehensive crystallographic analysis by: determining all space group symmetry operations of the crystal structure, and identifying the specific point group symmetry at each inequivalent atomic site.

The KGEN module generates the k-point mesh within the irreducible wedge of the first Brillouin zone, following the crystal symmetry operations determined by SYMMETRY.

DSTART generates the initial electronic charge density through superposition of atomic densities.

2.8.2. Self-consistent Field (SCF) Calculation

The self-consistent field (SCF) cycle is initiated and iteratively repeated until convergence criteria are satisfied. Each iteration consists of two hierarchically organized computational steps: (1) numerical solution of Eq. (II.46) to determine the expansion coefficients C G (as defined in Eq. II.53), followed by (2) calculation of the self-consistent electron density. This sequential procedure ensures systematic convergence of both wavefunction coefficients and charge density distribution. Thus, each iteration cycle comprises the following sequential steps:

- The LAPW0 module calculates the total effective potential by combining: (i) the Hartree potential, obtained through numerical solution of Poisson's equation, and (ii) the exchange-correlation potential, computed using either the generalized gradient approximation (GGA) or local density approximation (LDA).
- The LAPW1 module computes the Hamiltonian matrix elements and overlap matrix in the LAPW basis, followed by eigenvalue determination through matrix diagonalization.
- The LAPW2 module performs two critical functions: (1) determination of the Fermi energy level (E_F) and (2) computation of the valence electron charge density .
- The LCORE module performs relativistic calculations of core states within muffin-tin spheres, considering exclusively the spherical component of the potential.
- The MIXER module computes the new electron density by summing core and valence densities. However, this raw density is not directly used as input for the next cycle. Instead, it undergoes mixing with densities from previous iterations through an appropriate algorithm. The simplest scheme, developed by Pratt [97], employs a linear combination of the new density (ρ_{new}) with the previous iteration's density (ρ_{old}):

$$\rho_{new}(r) = (1-\alpha)\rho_{old}(r) + \left(\rho_c(r) + \rho_v(r)\right) \qquad \text{II-46}$$

α being the mixing parameter. As previously stated, self-consistency is achieved when the new density, obtained after the cycle, matches the input density.

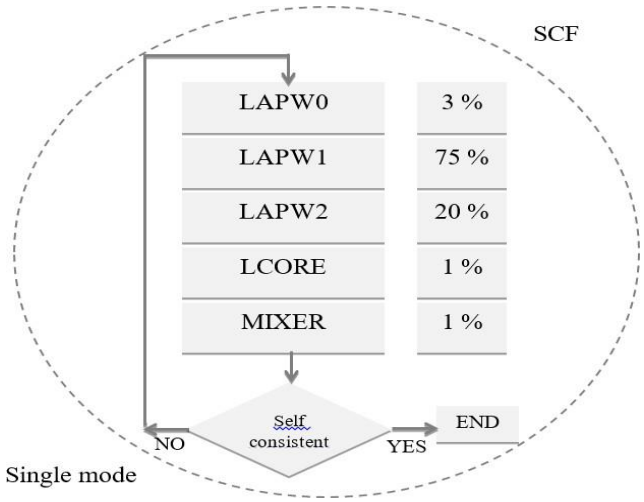

Figure 2.2: Diagram of an SCF cycle

2.8.3. Property Calculation

Physical property calculations are performed using the following programs:

- OPTIMISE determines the total energy as a function of volume, which is used to calculate the lattice parameter, bulk modulus, and its pressure derivative.
- TETRA computes the total and partial densities of states.
- SPAGHETTI computes the band structure using the eigenvalues generated by LAPW1.
- OPTIC computes the optical properties.
- XSPEC computes the absorption and emission X-ray spectral structures.

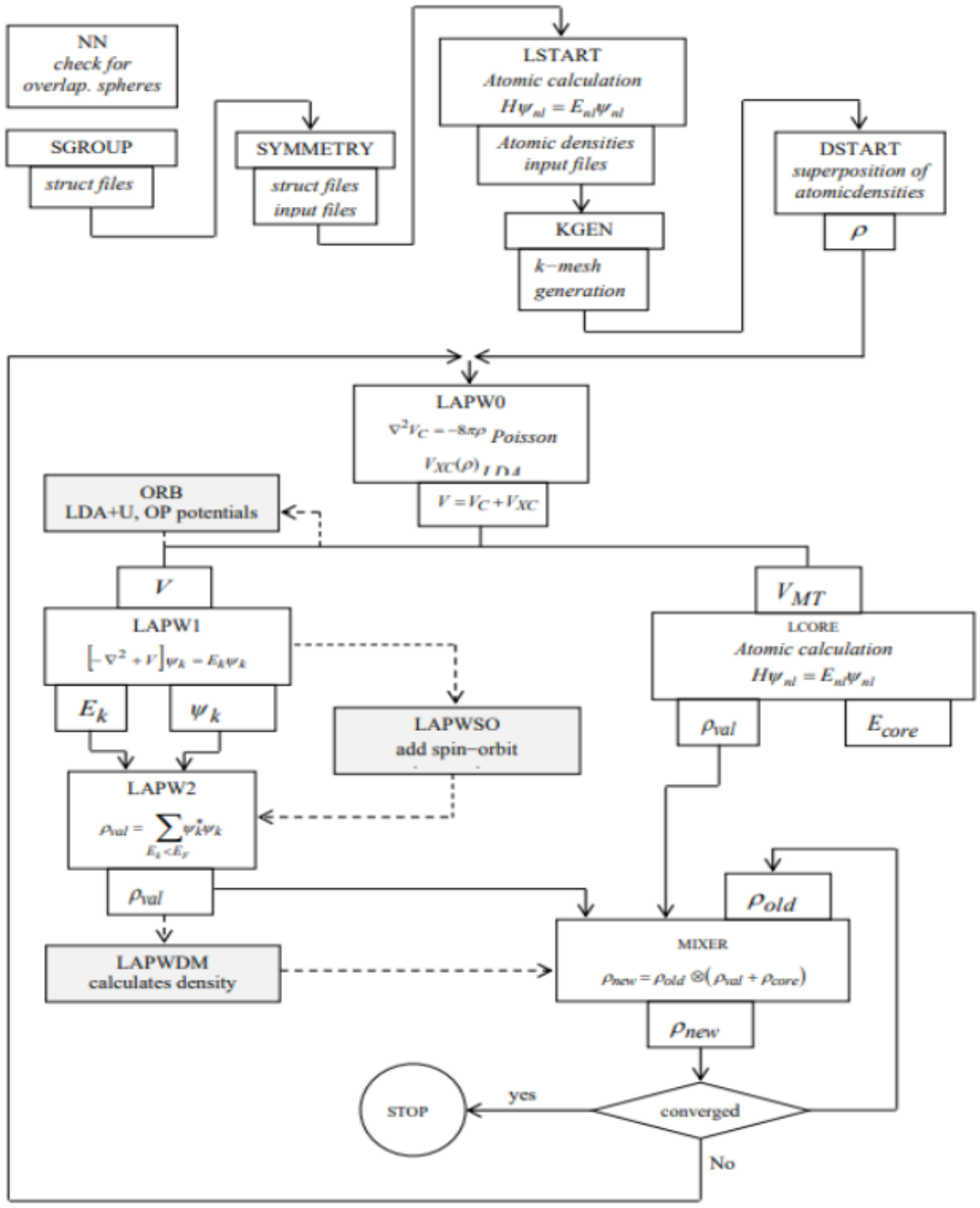

Figure 2.3: Computational Workflow of the WIEN2k Program

RESULTS AND DISCUSSIONS

3.1.Introduction

In this chapter, we present the results of our calculations concerning the structural, electronic and magnetic properties of the normal spinel Co_2MnO_4. We calculated the total energy as a function of volume, with all calculations performed assuming a cubic crystal structure. These calculations were carried out using the full-potential linearized augmented plane wave (FP-LAPW) method [96], as implemented in the WIEN2k code [37]. To account for exchange-correlation effects, we employed the generalized gradient approximation (GGA-PBE) as developed by Perdew, Burke, and Ernzerhof [38] method. This approach is based on density functional theory (DFT) [98]. Initially, our work focused on determining the physical properties of the spinel compound Co_2MnO_4.

3.2.Physical Properties of the Spinel CO_2MnO_4

3.2.1. Calculation Details

In the first part of this study, numerical simulations were performed based on a fundamental principle—density functional theory (DFT) [98]. These simulations were carried out using the full-potential linearized augmented plane wave (FP-LAPW) method [1], as implemented in the WIEN2k software package[37]. To ensure the accuracy of the calculations, optimized muffin-tin sphere radii (RMT) were selected: 2 atomic units (a.u.) for Manganese (Mn), 1.44 a.u. for oxygen (O), and 1.89 a.u. for Cobalt (Co). Additionally, a Brillouin zone sampling grid of 800 k-points was employed. To ensure reliable and physically meaningful results, stringent convergence criteria were rigorously enforced, including a total energy convergence threshold of 1.0×10^{-6} eV/atom, a force convergence criterion of 0.002 eV/Å**,** and a maximum ionic displacement tolerance of 1.0×10^{-4} Å**,** ensuring both electronic and structural optimization stability in the calculations. To accurately describe exchange-correlation interactions, the Perdew-Burke-Ernzerhof generalized gradient approximation (GGA-PBE)[38]was employed as the baseline functional.

3.2.2. Structural Properties

The material Co_2MnO_4 crystallizes in a normal spinel structure (cubic), characterized by the space group $Fd\bar{3}m$ (No. 227). In this structure, **Mn** atoms occupy the tetrahedral sites with atomic coordinates (3/8, 3/8, 3/8), while **Co** atoms are located at the octahedral sites with coordinates (0, 0, 0). Oxygen (**O**) atoms are positioned at face-centered cubic sites, defined by atomic coordinates (u, u, u). The arrangement of oxygen atoms in Co_2MnO_4 was determined through energy minimization calculations, yielding optimal coordinates of (0.26, 0.26, 0.26) for each oxygen atom. This atomic configuration is illustrated in **Figure III.1**.

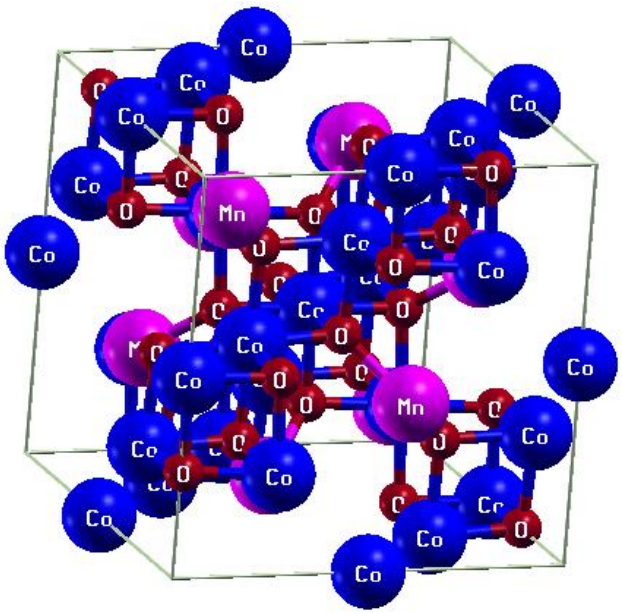

Figure 03.1: Crystal structure of the spinel Co_2MnO_4

To investigate the structural properties of Co_2MnO_4, calculations were performed to determine the relationship between the total energy (E) and the unit cell volume (V) under a specific magnetic configuration.

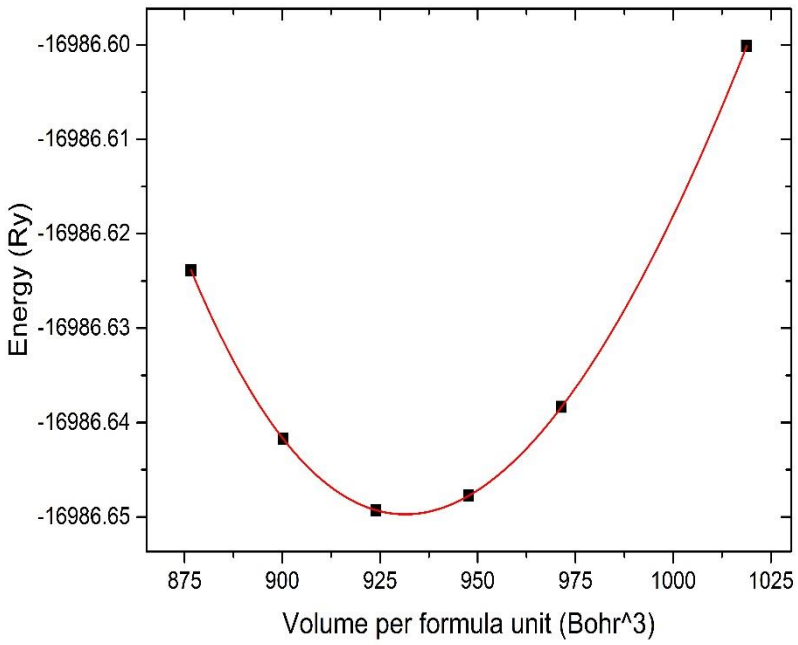

Figure 3.2: Total energy per formula unit of ferromagnetic (FM) phase as functions of the volume for Co_2MnO_4 compound.

To determine the structural ground state, such as the equilibrium lattice parameter (a_0), equilibrium unit cell volume (V_0), minimum total energy (E_0), bulk modulus (B), and its first derivative (B′), the calculated E–V data were fitted to the Birch-Murnaghan equation of state. A summary of these properties is presented in Table III-1, which also provides a comparison between the present results and this reported in previous study on Co2MnO4 [99].

Table III-1: Calculated lattice parameter (in Bohr), bulk modulus (in GPa), its derivative pressure, and energy (in Ry) for the structural and magnetic ground phase (FM) in Co_2MnO_4 compound.

Compounds	a_0	B	B'	E_{min}
Co_2MnO_4	15.5025 15.6280[99]	210.5196	4.6307	-16986.649697

3.2.3. Electronic Properties

We calculated the spin-polarized band structure of the normal spinel Co_2MnO_4 in its stable phase, the FM configuration, using GGA approach. The resulting band structures,

computed along high-symmetry directions of the Brillouin zone, are shown in Figure III-3 (a, b).

Using the GGA-PBE approach, the energy bands corresponding to the d states of Co are occupied in both spin-up and spin-down directions and are predominantly located above the Fermi level.

Using this approximation, the calculated indirect band gap (L-X) is 0.951 eV for the spin-down channel. Such characteristics may be of interest for applications in semiconductor field-effect transistors (FETs) and spintronic devices. Consequently, this new configuration exhibits half-metallic behavior.

To gain a deeper understanding of the impact of various electronic states on the band structure, total density of states (DOS) and partial density of states (PDOS) were calculated with spin polarization for the spinel Co_2MnO_4. The DOS and PDOS spectra computed using both GGA approach for Co_2MnO_4 are shown in Figure III-4.

By comparing the DOS and PDOS spectra obtained via the GGA method for the FM phase of the Co_2MnO_4 spinel, we observe that in the spin-up channel, the valence states are partially filled and cross the Fermi level, indicating a metallic character. However, in the spin-down channel, the valence states are partially filled but do not cross the Fermi level, indicating a semiconducting character. For that we can introduce our compound as “half-metal”.The PDOS spectra in the region around the Fermi level are predominantly governed by the 3d states of Mn atoms, which play a key role in determining the observed electronic and magnetic properties. In contrast, the contribution from the O 2p states is negligible. For the 3d and 4s states of Co, both the spin-up and spin-down states are fully occupied, but are confined to the lower energy region (approximately between –5.8 and –7 eV). Therefore, the magnetism observed in the spinel Co_2MnO_4 arises primarily from the 3d electrons of the Mn atoms.

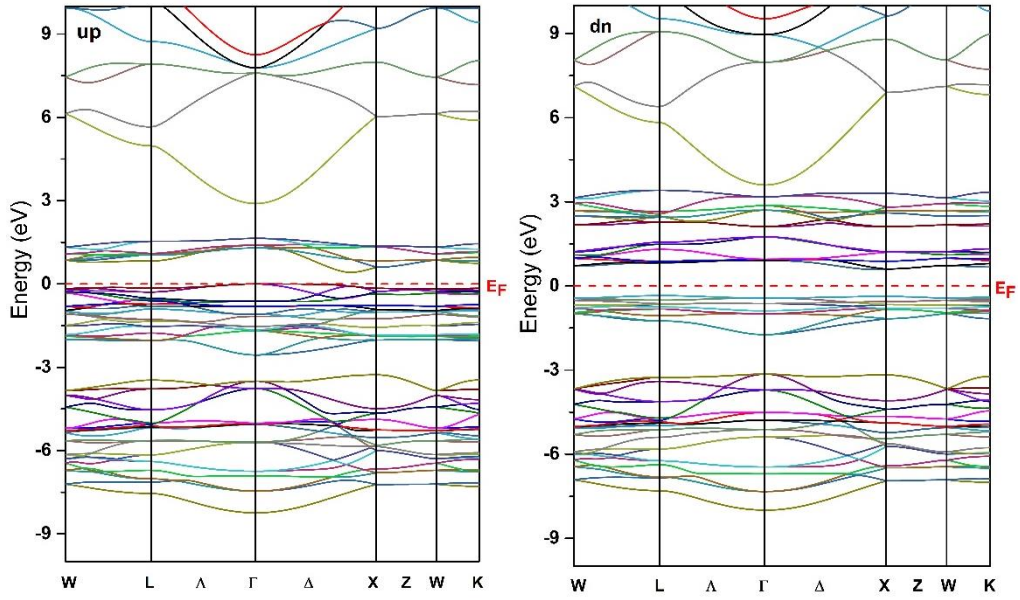

Figure 03.3: Spin-polarized band structures for Co2MnO4 compound.

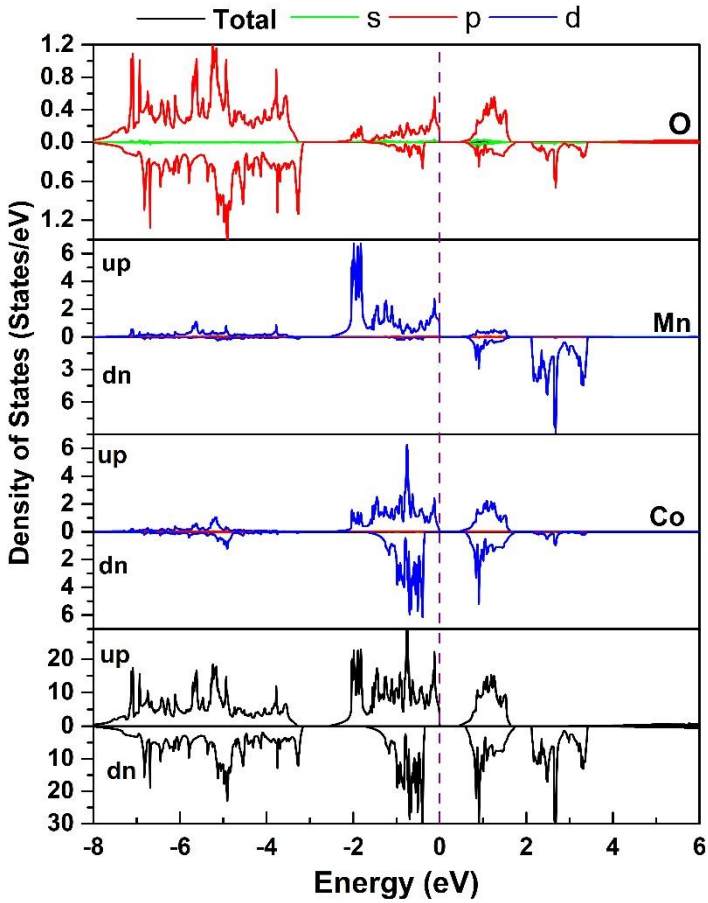

Figure 03.4: Spin-polarized density of states (DOS) for Co2MnO4 compound

3.2.4. Magnetic Properties

To gain a deeper understanding of the magnetic characteristics of the normal spinel Co_2MnO_4 and the interactions between its constituent atoms under the correlation potential GGA, the total and partial atomic magnetic moments were calculated and are presented in Table III-2. At first glance, the results indicate that the Mn atom exhibits a significant magnetic moment, while the contributions from Co and O atoms are comparatively minor in GGA approximation.

Table III- 2: Total (Mtot), Atomic (M_{Co}, M_{Mn}, M_O), and interstitial (MIntersti) magnetic moments (in μ_B) for Co_2MnO_4 compound.

M_{tot}	M_{Co}	M_{Mn}	M_O	$M_{Intersti}$
10.00	0.32831	3.72845	0.01959	1.07314

A total magnetic moment equal 10 suggests that the spin interactions are in **high-spin states**, indicative of ferromagnetic coupling between the magnetic sublattices.

GENERAL CONCLUSION

GENRAL CONCLUSION

This dissertation presented a comprehensive theoretical investigation of the normal spinel compound Co_2MnO_4 using first-principles calculations based on density functional theory (DFT) within the FP-LAPW method, as implemented in the WIEN2k code. The objective was to explore the structural, electronic, and magnetic properties of Co_2MnO_4 in order to assess its potential for spintronic applications.

Structural optimization confirmed the thermodynamic stability of Co_2MnO_4 in the cubic spinel phase, adopting the normal spinel configuration, in which Mn atoms occupy the tetrahedral sites and Co atoms reside in the octahedral sites. The obtained structural parameters and atomic arrangement were consistent with known characteristics of normal spinel oxides.

The electronic band structure revealed a half-metallic behavior, characterized by metallic conductivity in the majority spin channel and an indirect band gap of approximately 0.95 eV in the minority spin channel. This full spin polarization at the Fermi level is a key feature for spintronic functionality, as it enables spin-polarized charge transport essential for devices such as spin valves and magnetic tunnel junctions.

Magnetic property calculations reveal a total magnetic moment of 10 μ_B per formula unit. This magnetism predominantly originates from the 3d orbitals of Mn atoms occupying the octahedral sites, which exhibit strong spin polarization. In contrast, Co atoms located in the tetrahedral sites contribute a smaller magnetic moment but align ferromagnetically, reinforcing the overall magnetic ordering of the system.

Although this study did not include calculations of elastic, phononic, or optical properties, the results provide a robust theoretical foundation. The observed half-metallicity, high spin polarization, and ferromagnetic nature of Co_2MnO_4 suggest that it is a strong candidate for application in next-generation spintronic technologies.

Future investigations could include the effects of cation substitution, pressure, or temperature on the material's physical properties. Moreover, experimental synthesis and characterization—such as XRD, magnetometry, and transport measurements—would be crucial to validate the predicted behavior and to explore its practical integration into spintronic devices.

GENRAL CONCLUSION

In summary, this work offers valuable insights into the intrinsic physical properties of Co_2MnO_4 in its normal spinel form and reinforces its potential as a functional material in the growing field of spintronics.

REFERENCES

1. Liu, G., et al., *Thermodynamics and electronic structure characteristics of MFe2O4 with different spinel structures: A first-principles study.* Ceramics International, 2023. **49**(18): p. 29747-29754.
2. Flores-Lasluisa, J.X., et al., *Transition metal oxides with perovskite and spinel structures for electrochemical energy production applications.* Environmental Research, 2022. **214**: p. 113731.
3. Xu, H., et al., *Current and future trends for spinel-type electrocatalysts in electrocatalytic oxygen evolution reaction.* Coordination Chemistry Reviews, 2023. **475**: p. 214869.
4. Salih, S.J. and W.M. Mahmood, *Review on magnetic spinel ferrite (MFe2O4) nanoparticles: From synthesis to application.* Heliyon, 2023. **9**(6).
5. Sharma, A., *Influence of different substitution metal ion on magnetic properties of Mn-Zn ferrite.* Materials Today: Proceedings, 2021. **37**: p. 3058-3060.
6. Hema, E., et al., *The role of Mn2+-doping on structural, morphological, optical, magnetic and catalytic properties of spinel ZnFe2O4 nanoparticles.* Journal of nanoscience and nanotechnology, 2016. **16**(6): p. 5929-5943.
7. Bouhemadou, A., et al., *Electronic, optical, elastic, thermoelectric and thermodynamic properties of the spinel oxides ZnRh2O4 and CdRh2O4.* Journal of Alloys and Compounds, 2019. **774**: p. 299-314.
8. Patil, R., et al., *Synthesis, structural and magnetic properties of different metal ion substituted nanocrystalline zinc ferrite.* Results in Physics, 2013. **3**: p. 129-133.
9. Muscas, G., et al., *Magnetic interactions versus magnetic anisotropy in spinel ferrite nanoparticles.* IEEE Magnetics Letters, 2019. **10**: p. 1-5.
10. Miao, Q., et al., *Magnetic properties of N-doped graphene with high Curie temperature.* Scientific reports, 2016. **6**(1): p. 21832.
11. Trukhanov, A., et al., *Correlation between the composition, structural parameters and magnetic properties of spinel-based functional nanocomposites.* Nano-Structures & Nano-Objects, 2023. **33**: p. 100941.
12. Tatarchuk, T., et al. *Spinel ferrite nanoparticles: synthesis, crystal structure, properties, and perspective applications*. in *Nanophysics, Nanomaterials, Interface Studies, and Applications: Selected Proceedings of the 4th International Conference Nanotechnology and Nanomaterials (NANO2016), August 24-27, 2016, Lviv, Ukraine*. 2017. Springer.
13. Channa, N., et al., *Nickel-substituted manganese spinel ferrite nanoparticles for high-frequency applications.* Journal of Materials Science: Materials in Electronics, 2020. **31**: p. 1661-1671.
14. Jouini, A., et al., *Optical properties of transition metal ion-doped MgAl2O4 spinel for laser application.* physica status solidi c, 2007. **4**(3): p. 1380-1383.
15. Gonçalves, J.M., et al., *Feasible strategies to promote the sensing performances of spinel MCo 2 O 4 (M= Ni, Fe, Mn, Cu and Zn) based electrochemical sensors: a review.* Journal of Materials Chemistry C, 2021. **9**(25): p. 7852-7887.
16. Amani, S., et al., *Synthesis and investigation of CoMnFeO4/reduced graphene oxide as ecofriendly electrode material for supercapacitor and its electrochemical performances.* Journal of Alloys and Compounds, 2023. **937**: p. 168020.

17. El Abboubi, M. and S.E. San, *Integration of spinel ferrite magnetic nanoparticles into organic solar cells: a review.* Materials Science and Engineering: B, 2023. **294**: p. 116512.
18. Maksoud, M.A., et al., *Antibacterial, antibiofilm, and photocatalytic activities of metals-substituted spinel cobalt ferrite nanoparticles.* Microbial pathogenesis, 2019. **127**: p. 144-158.
19. Nandwana, V. and V.P. Dravid, *Multicomponent magnetic spinels: From complexity of crystal chemistry to coupled magnetic resonance imaging (MRI).* APL Materials, 2023. **11**(5).
20. Stevanovic, V., M. d'Avezac, and A. Zunger, *Simple point-ion electrostatic model explains the cation distribution in spinel oxides.* Phys. Rev. Lett, 2010. **105**(7): p. 11-14.
21. Nishikawa, S., *Structure of some crystals of spinel group.* Proceedings of the Tokyo Mathematico-Physical Society. 2nd Series, 1915. **8**(7): p. 199-209_1.
22. Barth, F. and E. Posnjak, *Silicate structures of the cristobalite type: I. The crystal structure of α-carnegieite (NaAlSiO4).* Zeitschrift für Kristallographie-Crystalline Materials, 1932. **81**(1-6): p. 135-141.
23. Zhang, G., A. Goldstein, and Y. Wu, *Novel transparent MgGa2O4 and Ni2+-doped MgGa2O4 ceramics.* Journal of Advanced Ceramics, 2022. **11**(3): p. 470-481.
24. Saei, J.N. and K. Asadpour-Zeynali, *Enhanced electrocatalytic activity of fluorine doped tin oxide (FTO) by trimetallic spinel ZnMnFeO4/CoMnFeO4 nanoparticles as a hydrazine electrochemical sensor.* Scientific Reports, 2023. **13**(1): p. 12188.
25. Divya, S., et al., *Impact of Zn doping on the dielectric and magnetic properties of CoFe2O4 nanoparticles.* Ceramics International, 2022. **48**(22): p. 33208-33218.
26. Kocevski, V., G. Pilania, and B.P. Uberuaga, *High-throughput investigation of the formation of double spinels.* Journal of Materials Chemistry A, 2020. **8**(48): p. 25756-25767.
27. Dos Santos, M.E., et al., *Mechanosynthesis of the multiferroic cubic spinel Co2MnO4: Influence of the calcination temperature.* Ceramics International, 2014. **40**(5): p. 7185-7193.
28. Rajeevan, N., et al., *Structural, electrical and magnetic properties of Bi-substituted Co2MnO4.* Materials Science and Engineering: B, 2009. **163**(1): p. 48-56.
29. Dos Santos, M.E., et al., *Cation distribution and magnetic characterization of the multiferroic cobalt manganese Co2MnO4 spinel doped with bismuth.* Journal of magnetism and magnetic materials, 2013. **329**: p. 53-58.
30. Dos Santos, M., et al., *Intrinsic magnetic properties of BixCo2− xMnO4 spinels obtained by short-time etching.* Journal of magnetism and magnetic materials, 2013. **339**: p. 157-162.
31. White, W. and B. DeAngelis, *Interpretation of the vibrational spectra of spinels.* Spectrochimica Acta Part A: Molecular Spectroscopy, 1967. **23**(4): p. 985-995.
32. Hosseini, S., et al., *Nanocrystalline AMn2O4 (A= Co, Ni, Cu) spinels for remediation of volatile organic compounds—synthesis, characterization and catalytic performance.* Ceramics International, 2012. **38**(2): p. 1655-1661.
33. Mendonca, M., et al., *Preparation and characterisation of spinel oxide ferrites suitable for oxygen evolution anodes.* Solid state sciences, 2002. **4**(2): p. 175-182.
34. Rajeevan, N., et al., *Magnetoelectric behavior of ferrimagnetic BixCo2− xMnO4 (x= 0, 0.1 and 0.3) thin films.* Journal of magnetism and magnetic materials, 2011. **323**(13): p. 1760-1765.

35. Blanco-Gutierrez, V., et al., *Neutron diffraction study and superparamagnetic behavior of ZnFe2O4 nanoparticles obtained with different conditions.* Journal of Solid State Chemistry, 2011. **184**(7): p. 1608-1613.
36. Cheng, F. and J. Chen, *Metal–air batteries: from oxygen reduction electrochemistry to cathode catalysts.* Chemical Society Reviews, 2012. **41**(6): p. 2172-2192.
37. Schwarz, K. and P. Blaha, *Solid state calculations using WIEN2k.* Computational Materials Science, 2003. **28**(2): p. 259-273.
38. Perdew, J.P., K. Burke, and M. Ernzerhof, *Generalized gradient approximation made simple.* Physical review letters, 1996. **77**(18): p. 3865.
39. Tropf, W.J. and M.E. Thomas, *Magnesium aluminum spinel (MgAl2O4),* in *Handbook of Optical Constants of Solids*1998, Elsevier. p. 883-897.
40. Szotek, Z., et al., *Electronic structures of normal and inverse spinel ferrites from first principles.* Physical Review B—Condensed Matter and Materials Physics, 2006. **74**(17): p. 174431.
41. Pénicaud, M., et al., *Calculated electronic band structure and magnetic moments of ferrites.* Journal of Magnetism and Magnetic Materials, 1992. **103**(1-2): p. 212-220.
42. Hosseini, S., *Structural, electronic and optical properties of spinel MgAl2O4 oxide.* physica status solidi (b), 2008. **245**(12): p. 2800-2807.
43. Mapossa, A.B., et al., *Removal of organic dyes from water and wastewater using magnetic ferrite-based titanium oxide and zinc oxide nanocomposites: a review.* Catalysts, 2021. **11**(12): p. 1543.
44. Hill, R.J., J.R. Craig, and G. Gibbs, *Systematics of the spinel structure type.* Physics and chemistry of minerals, 1979. **4**(4): p. 317-339.
45. Sickafus, K.E., J.M. Wills, and N.W. Grimes, *Structure of spinel.* Journal of the American Ceramic Society, 1999. **82**(12): p. 3279-3292.
46. Bhattacharya, J. and C. Wolverton, *Relative stability of normal vs. inverse spinel for 3d transition metal oxides as lithium intercalation cathodes.* Physical Chemistry Chemical Physics, 2013. **15**(17): p. 6486-6498.
47. Brabers, V., *Progress in spinel ferrite research.* Handbook of magnetic materials, 1995. **8**: p. 189-324.
48. Sundahl Jr, R. and Y. Kim, *Soft Magnetic Ferrites,* in *Concise Encyclopedia of Advanced Ceramic Materials*1991, Elsevier. p. 440-445.
49. Dastjerdi, O.D., H. Shokrollahi, and S. Mirshekari, *A review of synthesis, characterization, and magnetic properties of soft spinel ferrites.* Inorganic Chemistry Communications, 2023. **153**: p. 110797.
50. Dippong, T., E.A. Levei, and O. Cadar, *Recent advances in synthesis and applications of MFe2O4 (M= Co, Cu, Mn, Ni, Zn) nanoparticles.* Nanomaterials, 2021. **11**(6): p. 1560.
51. Narang, S.B. and K. Pubby, *Nickel spinel ferrites: a review.* Journal of Magnetism and Magnetic Materials, 2021. **519**: p. 167163.
52. Néel, L., *Antiferromagnetism and ferrimagnetism.* Proceedings of the Physical Society. Section A, 1952. **65**(11): p. 869.
53. Jiles, D.C. and D.L. Atherton, *Theory of ferromagnetic hysteresis.* Journal of magnetism and magnetic materials, 1986. **61**(1-2): p. 48-60.
54. Marrows, C., *Spin-polarised currents and magnetic domain walls.* Advances in Physics, 2005. **54**(8): p. 585-713.
55. Smart, J.S., *The Néel theory of ferrimagnetism.* American Journal of Physics, 1955. **23**(6): p. 356-370.

56. Burdett, J.K., G.D. Price, and S.L. Price, *Role of the crystal-field theory in determining the structures of spinels.* Journal of the american chemical society, 1982. **104**(1): p. 92-95.
57. Ali, S., et al., *Crystal field splitting, half metallic ferromagnetism, structural, mechanical and magneto-electronic properties of spinels type structure compounds MgX2O4 (X= Fe and Co) for spintronic applications.* The European Physical Journal Plus, 2021. **136**(7): p. 1-15.
58. Andreozzi, G.B., et al., *Color mechanisms in spinel: A multi-analytical investigation of natural crystals with a wide range of coloration.* Physics and Chemistry of Minerals, 2019. **46**: p. 343-360.
59. Kakol, Z., *Magnetic and transport properties of magnetite in the vicinity of the Verwey transition.* Journal of Solid State Chemistry, 1990. **88**(1): p. 104-114.
60. Goodenough, J.B., *The Verwey transition revisited*, in *Mixed-Valence Compounds: Theory and Applications in Chemistry, Physics, Geology, and Biology*1980, Springer. p. 413-425.
61. Acharya, N. and R. Sagar, *Structure and electrical properties characterization of NiMn2O4 NTC ceramics.* Inorganic Chemistry Communications, 2021. **132**: p. 108856.
62. Jagtap, S., et al., *Preparation, characterization and electrical properties of spinel-type environment friendly thick film NTC thermistors.* Journal of the European Ceramic Society, 2008. **28**(13): p. 2501-2507.
63. Reimann, T. and J. Töpfer, *Low-temperature sintered Ni–Zn–Co–Mn–O spinel oxide ceramics for multilayer NTC thermistors.* Journal of Materials Science: Materials in Electronics, 2021. **32**(8): p. 10761-10768.
64. Böer, K.W. and U.W. Pohl, *Magnetic Semiconductors*, in *Semiconductor Physics*2023, Springer. p. 319-365.
65. Goodenough, J.B., *Magnetic Semiconductors Intrigue Both Scientists and Engineers*, 1970, American Institute of Physics.
66. Dolgopolova, E.A., et al., *Strong Purcell enhancement at telecom wavelengths afforded by spinel Fe 3 O 4 nanocrystals with size-tunable plasmonic properties.* Nanoscale Horizons, 2022. **7**(3): p. 267-275.
67. Kumar, S. and R.R. Singh, *Ferrite nanoparticles for telecommunication application*, in *Engineered Ferrites and Their Applications*2023, Springer. p. 95-112.
68. Kaur, M. and S. Bahel, *Frequency and thickness dependent absorption analysis of pure and substituted Zn-Co spinel ferrites for radar applications.* Materials Today: Proceedings, 2024.
69. Xiang, N., et al., *The In Situ Preparation of Ni–Zn Ferrite Intercalated Expanded Graphite via Thermal Treatment for Improved Radar Attenuation Property.* Molecules, 2023. **28**(10): p. 4128.
70. Hill, M.D., D.B. Cruickshank, and I.A. MacFarlane, *Perspective on ceramic materials for 5G wireless communication systems.* Applied Physics Letters, 2021. **118**(12).
71. Gonçalves, J.M., et al., *Multifunctional spinel MnCo 2 O 4 based materials for energy storage and conversion: a review on emerging trends, recent developments and future perspectives.* Journal of Materials Chemistry A, 2021. **9**(6): p. 3095-3124.
72. Park, M.-S., et al., *Porous nanoarchitectures of spinel-type transition metal oxides for electrochemical energy storage systems.* Physical Chemistry Chemical Physics, 2015. **17**(46): p. 30963-30977.

73. Amiri, M., M. Salavati-Niasari, and A. Akbari, *Magnetic nanocarriers: evolution of spinel ferrites for medical applications.* Advances in colloid and interface science, 2019. **265**: p. 29-44.
74. Włodarczyk, A., et al., *Magnetite nanoparticles in magnetic hyperthermia and cancer therapies: Challenges and perspectives.* Nanomaterials, 2022. **12**(11): p. 1807.
75. Bernaoui, C.R., et al., *Synthesis and characterization of NiFe2O4 nanoparticles as reusable magnetic nanocatalyst for organic dyes catalytic reduction: study of the counter anion effect.* Materials Chemistry and Physics, 2022. **292**: p. 126793.
76. Iyyappan, J., et al., *Critical review on wastewater treatment using photo catalytic advanced oxidation process: Role of photocatalytic materials, reactor design and kinetics.* Case Studies in Chemical and Environmental Engineering, 2024. **9**: p. 100599.
77. Schrödinger, E., *An undulatory theory of the mechanics of atoms and molecules.* Physical review, 1926. **28**(6): p. 1049.
78. Sutcliffe, B.T., *The Born-Oppenheimer Approximation*, in *Methods in Computational Molecular Physics*1992, Springer. p. 19-46.
79. Hartree, D.R. *The wave mechanics of an atom with a non-Coulomb central field. Part I. Theory and methods*. in *Mathematical Proceedings of the Cambridge Philosophical Society*. 1928. Cambridge university press.
80. Grant, I., *Relativistic calculation of atomic structures.* Advances in Physics, 1970. **19**(82): p. 747-811.
81. Fock, V., *„Selfconsistent field "mit Austausch für Natrium.* Zeitschrift für Physik, 1930. **62**: p. 795-805.
82. Fock, V., *Näherungsmethode zur Lösung des quantenmechanischen Mehrkörperproblems.* Zeitschrift für Physik, 1930. **61**: p. 126-148.
83. Thomas, L.H. *The calculation of atomic fields*. in *Mathematical proceedings of the Cambridge philosophical society*. 1927. Cambridge University Press.
84. Görling, A., *Density-functional theory beyond the Hohenberg-Kohn theorem.* Physical Review A, 1999. **59**(5): p. 3359.
85. Gunnarsson, O., M. Jonson, and B. Lundqvist, *Descriptions of exchange and correlation effects in inhomogeneous electron systems.* Physical Review B, 1979. **20**(8): p. 3136.
86. Kohn, W. and L.J. Sham, *Self-consistent equations including exchange and correlation effects.* Physical review, 1965. **140**(4A): p. A1133.
87. Slater, J.C., *A simplification of the Hartree-Fock method.* Physical review, 1951. **81**(3): p. 385.
88. Ceperley, D.M. and B.J. Alder, *Ground state of the electron gas by a stochastic method.* Physical review letters, 1980. **45**(7): p. 566.
89. Perdew, J.P. and A. Zunger, *Self-interaction correction to density-functional approximations for many-electron systems.* Physical review B, 1981. **23**(10): p. 5048.
90. Perdew, J.P. and K. Burke, *Comparison shopping for a gradient-corrected density functional.* International journal of quantum chemistry, 1996. **57**(3): p. 309-319.
91. Dudarev, S.L., et al., *Electron-energy-loss spectra and the structural stability of nickel oxide: An LSDA+ U study.* Physical Review B, 1998. **57**(3): p. 1505.
92. Tran, F. and P. Blaha, *Accurate band gaps of semiconductors and insulators<? format?> with a semilocal exchange-correlation potential.* Physical review letters, 2009. **102**(22): p. 226401.

93. Lee, M.J. and V. Heine, *Different Types of Phase-Shift Pseudopotential with Application to the Alkali Metals and Copper.* Physical Review B, 1972. **5**(10): p. 3839.
94. Schwarz, K., P. Blaha, and G.K. Madsen, *Electronic structure calculations of solids using the WIEN2k package for material sciences.* Computer physics communications, 2002. **147**(1-2): p. 71-76.
95. Petersen, M., et al., *Improving the efficiency of FP-LAPW calculations.* Computer Physics Communications, 2000. **126**(3): p. 294-309.
96. Blaha, P., et al., *Full-potential, linearized augmented plane wave programs for crystalline systems.* Computer physics communications, 1990. **59**(2): p. 399-415.
97. Pratt Jr, G.W., *Wave functions and energy levels for cu+ as found by the slater approximation to the hartree-fock equations.* Physical Review, 1952. **88**(6): p. 1217.
98. Schwarz, K. and P. Blaha, *DFT calculations of solids in the ground state.* DFT calculations of solids in the ground state, De Gruyter, 2018: p. 67-100.
99. Brabers, V. and F. Van Setten, *X-ray photoelectron spectroscopy study of the ionic configuration of the spinel CuMnCoO4.* Journal of Physics D: Applied Physics, 1983. **16**(9): p. L169.

Abstract

This work presents a theoretical study of the normal spinel Co_2MnO_4 using density functional theory (DFT) within the FP-LAPW method as implemented in the WIEN2k code. Structural optimization confirms the stability of Co_2MnO_4 in the cubic spinel phase, where Mn atoms occupy the tetrahedral sites and Co atoms reside in the octahedral sites. Electronic structure calculations reveal a half-metallic character with an indirect band gap of 0.95 eV in the minority spin channel and full spin polarization at the Fermi level. The total magnetic moment is 10 μB per formula unit, mainly arising from Co 3d orbitals, indicating the material's ferrimagnetic nature. These results suggest that Co_2MnO_4 is a promising candidate for spintronic applications.

الملخص

يقدّم هذا العمل دراسة نظرية لمركب Co_2MnO_4 في بنيته السبينلية العادية باستخدام نظرية الكثافة الوظيفية (DFT)ضمن منهجية FP-LAPW كما هي مطبّقة في برنامج .WIEN2k أكّدت نتائج تحسين البنية استقرارية المركب في الطور المكعّب، حيث تشغل ذرات المنغنيز المواقع رباعية التناسق، في حين تشغل ذرات الكوبالت المواقع ثمانية التناسق. أظهرت الحسابات الإلكترونية أنّ المركب يتميز بخاصية نصف فلزية، مع فجوة طاقة غير مباشرة قدرها 0.95 إلكترون فولت في قناة اللف المغزلي الأقلية، واستقطاب كلي عند مستوى فيرمي. وقد تم حساب عزم مغناطيسي كلي قدرهμ_B 10 لكل وحدة صيغية، ويرجع أساسًا إلى إلكترونات 3 d للكوبالت، مما يدل على الطبيعة الفيريمغناطيسية للمركب. وتشير هذه النتائج إلى أن Co_2MnO_4 يعد مرشحًا واعدًا لتطبيقات الإلكترونيات المغزلية.(spintronics)

Résumé

Ce travail présente une étude théorique du composé spinelle normal Co_2MnO_4 en utilisant la théorie de la fonctionnelle de la densité (DFT) selon la méthode FP-LAPW, telle qu'implémentée dans le code WIEN2k. L'optimisation structurale confirme la stabilité du composé dans la phase cubique spinelle, où les atomes de Mn occupent les sites tétraédriques et ceux de Co les sites octaédriques. Les calculs de structure électronique révèlent un comportement demi-métallique avec une bande interdite indirecte de 0,95 eV dans le canal de spin minoritaire et une polarisation totale au niveau de Fermi. Le moment magnétique total est de 10 μ_B par unité formulique, provenant principalement des orbitales 3d du cobalt, ce qui confirme le caractère ferrimagnétique du composé. Ces résultats suggèrent que Co_2MnO_4 est un candidat prometteur pour les applications en spintronique.